Diplomarbeit

zur Erlangung des Titels "Diplomingenieur"

Development of an inductive measurement system based on a beat frequency oscillator to investigate particle mixing in circulating fluidized beds

Roland Schropp, BSc.

00940182

Betreuer:
Dipl.-Ing. Gerhard Hofer,
Univ.Prof. Dipl.-Ing. Dr. Tobias Pröll

November 14, 2018

Eidesstattliche Erklärung

Hiermit erkläre ich an Eides statt, dass ich die vorliegende Diplomarbeit selbständig und ohne fremde Hilfe verfasst, andere als die angegebenen Quellen und Hilfsmittel nicht benutzt und die den benutzten Quellen wörtlich und inhaltlich entnommenen Stellen als solche erkenntlich gemacht habe.

Affidavit

I declare in lieu of oath, that I wrote this thesis and performed the associated research myself, using only literature cited in this volume.

Acknowledgements

First of all, I want to express substantial amounts of dedication to Mr. David Smith and his one man business Essex Metal Detectors, as his inspiring and encouraging instructional website led to the decision to develop the device that really gave this thesis its purpose. This work would not have been possible without him.

Secondly, I want to thank Gerhard Hofer for being such an exceptionally devoted supervisor, always reacting instantly, friendly and more than competently to any problems his students would have and always taking the time they need. He made me think of the collaboration like it was an undeserved luxury.

Also, I want to thank all those colleagues at the University of life sciences, who helped me in the workshop and with their experiences on various topics, especially Florian Pröll, Florian Zerobin and Friedrich Kropitz.

I feel honored to thank Tobias Pröll, Professor at the Institute of Chemical and Energy Engineering for being such a highly respectful and caring head supervisor and scientific leader.

Another important individual to thank is Johannes Fuchs, as his major portions of the the design and making of the cold flow model device were done by him.

Further I highly appreciate the patience and cherishing emotional and financial support from my parents that enabled me to finish my Diploma Engineer degree course.

There also needs to be a place to thank Sabine Mansky, the one very special person in my life for all her patience and understanding at all the disagreements and the rocky road we walked since getting acquainted in our mutual study.

Abstract

A simple and low-cost beat frequency oscillator (BFO) device has been developed in this thesis that was capable of performing inductive measurements of residence time distribution (RTD) using ferromagnetic tracer particles in a cold flow model featuring a circulating fluidized bed (CFB).

The main bed material were glass beads sized 145 μm, spiked with ferritic stainless steel 1.4742 tracer particles of 45-100 μm in size.

The fluidized bed chamber had a footprint of 200 x 400 mm and a moving bed height of 300-400 mm and the bed was fluidized with velocities of up to 0.278 m/s.

Solids circulation in the particle loop was controlled by a screw conveyor, with mass flows of up to 210 kg/h.

The measurement coils were mounted at the particle inlet and outlet pipes and were used as frequency determining parts of LC-oscillators. The ferquency deflection was measured differentially from a beat wave with a reference oscillator according to the BFO principle.

Pulse injection RTD measurements were started with the removal of a magnet applied to the downcomer upstream of the inlet measurement coil.

The frequency deflection was correlated to mass fractions of tracer material inside a measurement coil, which proved to be a linear relation for mass fractions of up to 0.11 and the small residual error was non-systemic.

The minimum fluidization velocity u_{mf} was determined to be equal to the minimum bubbling velocity u_{mb} at 0.028 m/s and bubbling activity was shown to be more homogeneous in lower regions of the bed and more vigorously fluctuating close to the surface.

Excellent effective temporal resolution of the measurement method was shown with capturing the tracer injection peak, while problems related to signal drift were encountered during the longer termed RTD measurement.

Idealized reactor models were fitted to the RTD curve and the characteristics and deviations of the data were discussed.

Zusammenfassung

Im Rahmen dieser Diplomarbeit wurde ein einfacher und kostengünstiger Schwebungsfrequenzoszillator entwickelt, der es ermöglichte, durch induktive Messung von ferromagnetischen Tracerpartikeln, in einem Wirbelschicht-Kaltmodell mit Feststoffzirkulation Verweilzeitverteilungen aufzuzeichnen.

Das Bettmaterial bestand dabei hauptsächlich aus Glaskugeln mit mittleren Durchmessern von 145 μm und war mit Tracerpartikeln aus Stahl des Typs 1.4742 mit Korngrößen von 45-100 μm versetzt.

Das Wirbelbett hatte eine Grundfläche von 200 x 400 mm, eine Höhe von 300-400 mm und die maximale Fluidisierungsgeschwindigkeit betrug 0.278 m/s.

Die Zirkulation der Feststoffe durch eine Partikelschleife wurde mit einem Schneckenförderer auf bis zu 210 kg/h reguliert.

Messspulen an den Ein- und Ausgangsrohren der Wirbelkammer fungierten als frequenzbestimmende Komponenten von L/C-Oszillatorschaltungen. Die Frequenzänderung wurde je anhand der, durch Mischung mit dem Referenzsignal entstehenden Schwebung differenziell quantifiziert.

Um Verweilzeitmessungen zu starten, wurde das Tracermaterial mittels Entfernen eines Rückhaltemagneten am Downcomerrohr als Puls injiziert.

Die Frequenzänderung der Schwebungswelle war bei Tracerkonzentrationen bis 0.11 g/g linear und wies nur kleine Zufallsfehler auf.

Die Mindestfluidisierungsgeschwindigkeit u_{mf} entsprach der kleinsten blasenbildenden Fluidisierungsgeschwindigkeit u_{mb} und lag bei 0.028 m/s.

Weiters wurde gezeigt, dass sich die Tracerkonzentration nahe des Bodens eines blasenbildenden Wirbelbettes ruhiger verhält als in Oberflächennähe.

Kurzzeitmessungen zeigten die außerordentlich hohe zeitliche Auflösung dieser Messmethode, während bei längeren Messzeiten problematische Signaldrifts auftraten.

Idealisierte Reaktormodelle konnten an die RTD-Kurven angepasst und deren Parameter, sowie die sich daraus ergebenden Charakteristika der Anlage bestimmt werden.

Contents

1 Introduction **1**
1.1 Preliminaries 1
1.2 Problem Definition 2
1.3 Objectives of the Thesis 3

2 Theoretical Background **4**
2.1 Particle Characterization 4
2.1.1 Particle Size and Size Distributions 4
2.1.2 Particle Classification According to Geldart . 6
2.2 Fluidized Bed Fundamentals 8
2.2.1 Fluidization and Fluidization Velocity 8
2.2.2 Intermediate Fluidization Regimes 10
2.2.3 Entrainment of Solids 10
2.3 Residence Time Distributions and Reactor Characteristics 12
2.3.1 The Residence Time Distribution (RTD) . . . 12
2.3.2 The Idealized Plug Flow Reactor (PFR) . . . 15
2.3.3 Continuously Stirred Tank Reactor (CSTR) . 15
2.4 Inductive Measurement Principles 16
2.4.1 Static Electromagnetism 17
2.4.2 Electromagnetic Induction 18
2.4.3 Inductive Measurement of Ferromagnetic Tracer Particles 19
2.4.4 Principles of Beat Frequency Oscillation (BFO) 21
2.4.4.1 Principles of Electric Oscillatior Circuitry 21
2.4.4.2 The Beat Effect 22

3 Experimental Setup **23**
3.1 Particulate Solids used for the Measurements 23
3.2 Measurement Equipment 24
3.2.1 Beat Frequency Oscillator 24
3.2.1.1 Design of the Circuitry and Device . 26
3.2.1.2 Data Recording and Processing Procedure 28
3.2.2 Measurement Coils 31
3.2.3 Reference Coils 31

3.3 Calibration of the Measurement System 32
3.4 Small Scale Fluidization Pipe 33
3.5 Design of the Cold Flow Model 35
3.5.1 The Particle Loop Assembly 36
3.5.2 Pressurized Air Supply 38
3.6 Calibration of Particle Circulation Mass Flow 39
3.7 RTD Measurement Procedure 40

4 Results & Discussion 41
4.1 Calibration of the Particles Circulation Rate 41
4.2 Correlation of the BFO Frequency Deflection to the Relative Content of Steel Powder Within the Coil . . 42
4.3 Bed Expansion Measurements 44
4.4 RTD Measurements 46

5 Conclusions & Outlook 52
5.1 Suggestions for the Improvement of the Performance of the BFO Device 52
5.2 Suggestions for the Improvement of the Data Processing Procedure 53
5.3 Suggestions for the Improvement of the Calibration of the Particle Circulation Rate 53

6 Appendix 65

1 Introduction

1.1 Preliminaries

Fluidized beds are a key technology for the transfer of mass and heat between a particulate solid phase and a fluid phase [1, 2], with mass transfer either meaning sorption processes, coating or chemical reactions such as combustion, pyrolysis or gasification [3], along with a variety of chemical syntheses [1, 4].

Their applications cover a wide variety of fields of engineering and are encountered particularly in chemical and energy [5–7], but also in pharmaceutical, food, mining, metallurgy and polymer industries [1, 8].

However, the number and complexity of processes regarding fluid dynamics and particle movement, as well as the mechanical, thermal and chemical interactions within the reactor chamber, especially when combined with the high temperature and pressure conditions frequently encountered in real applications [9] make fluidized bed reactors a complicated subject to model and predict [1, 10, 11] and causes numerical simulations to become distinctly exhaustive [12].

Even further challenges arise from extending the investigation to the heat transfer between the bed and immersed surfaces [11, 13] and their influence on particle movement, both of which the cold flow model used in the practical part of this thesis was designed for (a detailed description of the device is given in section *3.5*). When portions of solid particles are continuously removed from either one side of a bubbling fluidized bed or from the top of a turbulently fluidized bed and fed back again, a CFB is established. In case of a bubbling fluidized bed, particle looping is achieved by pneumatic transport in a riser, separated from the fluidized bed by an air seal (e.g. particle siphon or screw conveyor). In any case, vertical particle transport is followed by a particle separator and free particle sedimentation in a downcomer pipe.

With the introduction of particle circulation, a lateral net movement of particles through the bed is the consequence, however, this does not mean there is a steady and calm flow of particles from the downcomer through the bed to the riser, as it has been shown by Yagi and Kunii [14] that CFBs are subject to complete mixing.

1.2 Problem Definition

It is imperative to understand the movement of particles through and their residence behavior in the fluidized bed in order to calculate and decide upon a reactor's flow requirements regarding solids feed, looping and drain streams. The acquisition of information on particle flow is one fundamental problem in the endeavor for reactor modeling and can be approached in a variety of ways.

Numerical simulations are the most "bottom up" approach available, predicting the mixing and drainage of particles from fulfilling basic physical equations that act on either individual particle bodies or a fluid-like particle mass within a frame of boundary conditions. While detailed information even on single-particle level can be accessed in such a way, correctness and reliability of the gained data have to be verified, thus experimental proof still is inevitable.

The most detailed (local) experimental information on particle flow can be derived from imaging methods based on the detection of the absorption of γ radiation [15]. However, safety and ethical concerns, cost, effort and European legislation strongly encourage the search for alternative methods.

Other than the mostly intrusive optical or even suction probing approaches described by J. Werther [15], inductive measurement can be applied from outside of piping sections, totally non-intrusively, yet they provide continuous operability at fast response characteristics [16].

However, the kind of measurable quantities are different for this technique too. These are limited to input/output mass balancing and therefore fall into the most "top down" category of measurement approaches. Rather than providing multivariate visual information, this method is limited to the detection of the collective amount of tracer particles within and around an inductor coil, i.e. a single value. Still, by placing coils at the riser and downcomer pipes and logging the time course of their inductivity after injection of a portion of ferromagnetic tracers into the downcomer and immediate magnetic recapturing of the tracers before they re-enter the downcomer coil, the RTD within the fluidized bed chamber can be calculated (see section *3.2* for a detailed explanation of the measurement setup).

Having identified inductive measurement as a sufficient, yet safe and relatively low cost and low effort measurement method then gave rise to the question which electronic principle to use for the measurement of the inductivity of the sensor coils.

Pulse induction metal detectors are said to have very good sensitivity and therefore low detection limits, however their working principle relies on the analysis of the time course of the magnetic field breakdown after each pulse, so the temporal resolution of this technique is limited [17]. In addition, problems with implementation of the signal into the routine of the programmable logic controller (PLU) of the cold flow model and problems related to logging of its data were feared and led to the decision of focusing on continuous wave types of metal detectors. So the design and optimization of suitable techniques for detection of ferromagnetic tracer particles was defined the major problem to be investigated in this thesis.

1.3 Objectives of the Thesis

The determination of fluidization parameters including the minimum fluidization velocity u_{mf} and minimum bubbling velocity u_{mb} for the classification of the main bed material according D. Geldart [18] was defined a first preliminary objective.

Further, the calibration of the solids circulation rate in the particle loop of the cold flow model was another preliminary objective.

The most central objective was the development and implementation of an inductive measurement system for ferromagnetic tracer particles suitable for the recording of data that could be used for the calculation of residence time distributions. Inquiries regarding existing systems for the same particular purpose on the one hand and metal detectors in general on the other hand led to the decision of investigating a BFO (see section *3.2* for detailed explanation of the circuitry and peripheral components of the device) - to my knowledge for the first time - to be used as a frequency based system for inductive tracer detection in fluidized bed equipment.

With the system working qualitatively, the first sub-objective was to investigate the linearity and reliability of the frequency deflection in a series of calibration measurements.

Further, a series of inductive bed expansion measurements with a bench top fluidization chamber featuring a tracer spiked bed was defined another minor objective. Bubbling activity was to be observed and characterized with the measurement coil being placed in 2 distinct height positions: close to the bottom of the bed, "low", and close to the bed surface, "high".

Finally, the recording of tracer curves to verify function of the system in-situ as well as its fitness for the purpose of calculating residence time distributions was defined the objective with the highest priority. Idealized models were to be chosen and/or combined and fitted to a measured RTD to identify and quantify characteristic properties of the behavior of the cold flow model.

2 Theoretical Background

2.1 Particle Characterization

As fluidized beds do have a wide range of uses and the nature of the participating solids can vary greatly throughout the spectrum of applications, a closer look at the properties of particles will be beneficial.

The most important parameters for particle characterization will be the mean or equivalent particle diameter d_p, a shape correction factor ϕ and the particles' inner density ρ_p.

Further parameters of interest are the voidage ratio ϵ and the bulk density ρ_b.

2.1.1 Particle Size and Size Distributions

Depending on the characteristic shape of the particles, as well as on the width and shape of their size distribution and purpose of the application, different approaches for determining an equivalent particle diameter can be helpful:

The equivalent particle diameter is calculated as the diameter of spheres d_V which occupy the same volume V_p (e.g. displace the same amount of liquid) as the same number of the actual particles:

$$d_V = \sqrt[3]{6V_p/\pi} \tag{1}$$

Since one of the sphere's geometrical properties is that it encloses a given volume exposing the least surface area possible in 3-dimensional space, the surface of a sphere equivalent in volume must be less or equal to the surface of the actual particles.

Especially for adsorption and other immediately surface-related processes, obviously equivalency related to surface area will be of interest. Hence, the respective equivalent particle diameter d_S is defined as the diameter of spheres that provide the same surface area A_p as the actual bed of particles:

$$d_S = \sqrt{A_p/\pi} \tag{2}$$

The most subtle yet simple - hence the most practical - equivalent sphere diameter is one that maintains the ratio of surface area to volume, as defined in (3).

$$\frac{d_{SV}^2\pi}{d_{SV}^3\pi/6} = \frac{A_p}{V_p} \Longrightarrow d_{SV} = \frac{6V_p}{A_p} \tag{3}$$

.

Also called the effective diameter, this is parameter is of great relevance for fluid flow through solid beds, since the surface is related to the drag force exerted on a particle when fluid is flowing by, while its volume directly relates to its weight force, so d_{SV} is already a good measure for the ease of overcoming the weight force, i.e. of fluidizing these particles.

Further, a shape factor can be introduced, that is defined as shown in (4),

$$\phi = \frac{A_{S,Veq}}{A_p} \tag{4}$$

where $A_{s,Veq}$ is the surface area of a sphere with a volume equivalent to that of an average particle. Aside from providing a convenient measure for particles' sphericity, it also helps to transform aforementioned diameters into each other [19].

In practical situations, the mean Sauter diameter $\bar{d_p}$ can be acquired through sieving Analysis using (5),

$$\bar{d_p} = \frac{1}{\sum\limits_i^n \frac{x_i}{d_i}} \tag{5}$$

where x_i is the mass fraction retained in the i^{th} sieve interval of n total sieve intervals and d_i is the mesh size of that sieve interval.

Then the mean $\bar{d_{SV}}$ is calculated from the mean Sauter diameter using (6).

$$\bar{d_{SV}} = \phi * \bar{d_p} \tag{6}$$

When particles are randomly poured into a vessel to form a bed, inter-particle spaces will be contained in the bed volume for 2 reasons: firstly, most particles are shaped in a way that prohibits voidless assembly merely by their geometry. But even if particles had perfect geometry allowing for voidless assembly, they secondly are very unlikely to do so due to friction forces and local optima of geometrical arrangements that occur from random pouring. The voidage or voidage ratio ϵ results from relating the void volume, defined as the bed volume that is not occupied by particles, to the total bed volume, as shown in (7),

$$\epsilon = \frac{V_{void}}{V_{bed}} \tag{7}$$

with V_{void} being the volume occupied by the inter particle space and V_{bed} being the total bed volume.

Since the void volume is where the gas flow mainly occurs, this parameter has great importance for characterization and calculation fluidized beds.

Directly related to the voidage ratio and particle density is the bulk density ρ_b, defined by (8) for $\rho_p >> \rho_f$,

$$\rho_b = \frac{m_{bed}}{V_{bed}} = \rho_p \cdot (1 - \epsilon) \tag{8}$$

with m_{bed} being the weight of a fixed bed volume V_{bed}, ρ_f being the density of the fluid and ρ_p being the intra particle density.

2.1.2 Particle Classification According to Geldart

One further useful and well established way of characterizing collective particle masses is the classification according to D. Geldart [18]. Thereby, fluidization behavior of particle beds is divided into 4 classes denoted by the letters A through D by specific criteria:

Class A particles can be fluidized without bubble formation, e.g. have a minimum fluid velocity u_{mb} at which bubble formation occurs that is higher than the minimum fluidization velocity u_{mf} ($u_{mb} > u_{mf}$).

Class B particles have a minimum bubbling velocity lower or equal to the minimum fluidization velocity and therefore begin to form bubbles directly at their fluidization ($u_{mb} \leq u_{mf}$).

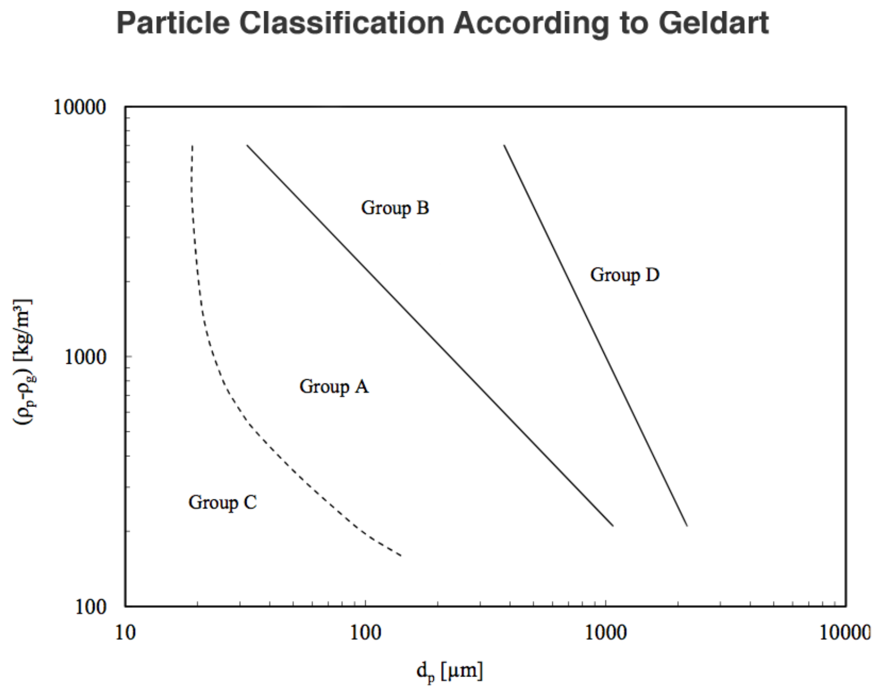

Figure 1: Geldart particle regimes and their discrimination conditions in 2 dimensional field of density difference between particles and fluid versus particle size.

Class C particles have the peculiarity of non-negligible to even strong inter particle forces that hamper thorough fluidization and mixing, but tend to form more or less static channels through which the gas flows without interfering much with the bed. Those inter particle forces are mostly due to either electro static charging of the particles at insulating vessel walls, or excessive moisture of the particles, sticking to each other by mediation of a more or less cohesive liquid. The first Problem can be overcome by coating of either vessel walls or particles with conductive layers and moisturizing of the fluidization gas, while the second can be approached by either exploiting the possibilities of reducing the moisture before fluidization or adding stirrers or vibrating baffles in the fluidization chamber.

Class D particles are particularly large or dense or both, so with this strong weight to surface ratio gas flow through bed must have high velocities and might already be turbulent before fluidization occurs. In this class, all bubbles move slower than the gas inside unless very close to the bed surface.

A graphical convolution of those classes and their separation criteria is presented in Figure 1. However, since the criterion for particle to belong to class C is widely dependent on the strength of inter particle forces which the graph does not account for, this criterion is variable and could theoretically overrule any other class. The condition for separation of classes B and D is somewhat fuzzy and depends on rather complex criteria, hence detailed explanation will be omitted, while the criterion for the separation of classes A and B is discussed in their respective paragraphs above.

2.2 Fluidized Bed Fundamentals

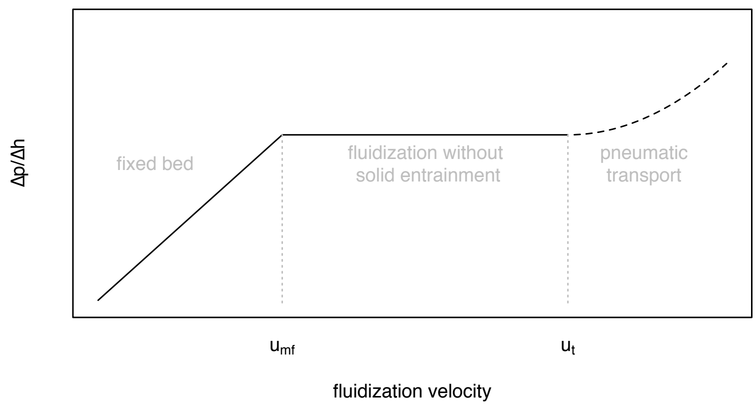

Figure 2: Progression of the pressure difference between the vertical bed limits through the stages of fluidization.

2.2.1 Fluidization and Fluidization Velocity

A loosely packed bed of particulate solid matter is fluidized when a fluid with a density lower than that of the particles is run through vertically from beneath in upwards direction at a velocity at which the drag force of the particles exceeds their weight force [3, 4, 20]. The empty conduit fluid velocity at which the particles' drag force exactly matches their weight is defined as the minimum fluidization velocity u_{mf} [1]. At velocities below that point, the bed remains a fixed bed [21], with each particle resting on its respective substructure. In this sub-fluidized region ($u_f < u_{mf}$), the back pressure of the bed increases quasi-linearly with increasing fluid velocities (see Figure 2) and bed height according to the Ergun-Equation (9), for cases where particle size is small and fluid velocity is low:

$$\frac{\Delta p}{\Delta h} = 150 \cdot \frac{(1-\epsilon)^2}{\epsilon^3} \cdot \frac{\mu \cdot u_f}{(\phi \cdot d_p)^2} + 1.75 \cdot \frac{1-\epsilon}{\epsilon^3} \cdot \frac{\rho_f \cdot u_f^2}{\phi \cdot d_p} \tag{9}$$

In this equation as well as in the following ones, Δp refers to the pressure drop measured at two height positions of the fixed bed, Δh is the height difference between the measurement positions, μ is the dynamic viscosity, ρ_f is the density of the fluid, ϕ is the surface related shape factor, d_p is the mean Sauter diameter as acquired from sieve analysis,

The condition for the state of minimum fluidization can be stated as the pressure difference through the bed matching the bed's weight force, as it is formally written in (10),

$$\frac{\Delta p}{\Delta h} = (1-\epsilon) \cdot (\rho_p - \rho_f) \cdot g \tag{10}$$

with g being the gravitational acceleration.

Wen and Yu [22] first proposed coefficients for the solution of the above equations in dimensionless numbers. J. R. Grace [23] posted more meaningful coefficients, as given in (11),

$$Re_{mf} = \sqrt{27,2^2 + 0.0408 \cdot Ar} - 27.2 \tag{11}$$

with Re being the Reynolds number, which is directly related to the particle size according to (12) (for the calculation of u_{mf} insert Re_{mf}) and Ar being the Archimedes number, a dimensionless variable which is calculated from fluid related as well as particle related properties according to (13).

$$Re = \frac{d_p * \rho_f * u_f}{\mu} \tag{12}$$

$$Ar = \frac{\rho_f \cdot d_p^3 \cdot (\rho_p - \rho_f) \cdot g}{\mu^2} \tag{13}$$

In the equations mentioned above, d_p refers to the Sauter mean diameter, ρ_p and ρ_f are the densities of the particles and the fluid, μ is the viscosity of the fluid u_f is the superficial fluid velocity

Fluid velocities higher than u_{mf} cause the phenomenon of fluidization to appear, where a formerly fixed bed of solid particles takes on some properties of a liquid [20, 24, 25], such as reacting to pressure gradients with respective flow patterns [25] maintaining a level upper surface, even throughout separate vessels sharing only a submerged connection, jet shaped gushing of particle mass out of a hole in a vessel or floating of relatively light and submersion and sinking of relatively heavy objects [24].

2.2.2 Intermediate Fluidization Regimes

After raising the fluid velocity beyond u_{mf} and u_{mb}, fluidization and formation of bubbles and eventually slugs occurs. While a detailed explanation of the formation of bubbles and slugs is beyond the scope of this work, it should be mentioned here that these phenomena are a result of the fluid finding its way of the least static and dynamic resistance through the bed. As the size of the bubbles rises with increased fluid velocity, they are called slugs when their diameter rises towards the one of the vessel.

When the fluid velocity is further increased, the vigorous movement disrupts the slugs into a much less ordered, turbulent fluidization. In this regime, the top surface of the bed becomes increasingly fuzzy, with the onset of the entrainment of solids marking the transition to the fast fluidization regime. From the beginning of fluidization at u_{mf} to the occurrence of solid entrainment at u_t the back pressure generated by the bed is - although noisy - remarkably uniform when averaged, as it is depicted in Figure 2.

2.2.3 Entrainment of Solids

When the fluid velocity is high enough to create a drag force on the particle that exceeds its weight force not only in the voidage of the bed, but also in the free board, this particle is entrained by the fluid flow. In the fast fluidization regime, this happens at chance when a high velocity portion of fluid or a portion of high surface to volume ratio particles meet the requirement of sufficient upwards acceleration to entrain a portion of particles. Now, if the fluid velocity is raised to a degree where the vast majority of particles is entrained with the average empty conduit fluid velocity, the pneumatic transport regime is reached. As the name suggests, this regime has less importance for the fluidization of beds than for transport, as encountered e.g. in the riser of CFBs operated in fluidization regimes lower than fast fluidization, which is also the case for the cold flow model used in this thesis.

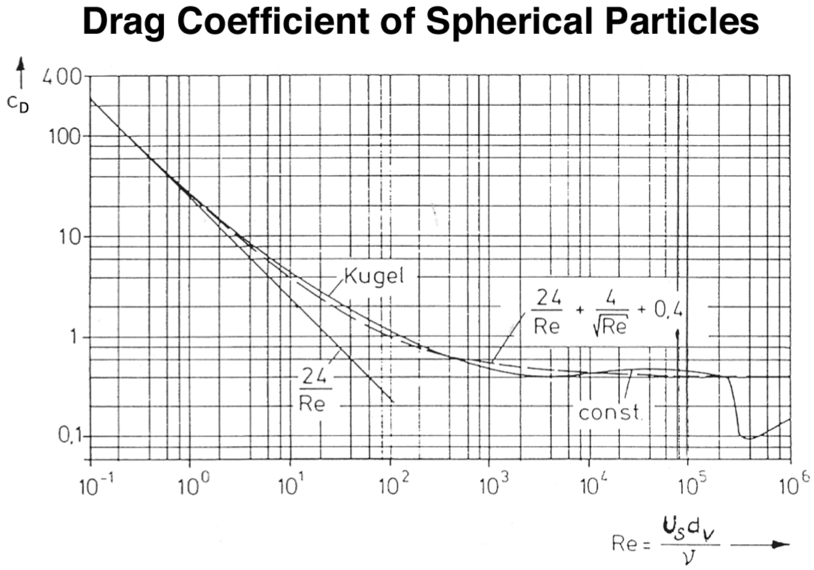

Figure 3: Drag coefficient in a range of particles' Reynolds numbers.

In terms of particle mechanics, the entrainment of solids is usually predicted by comparing the average superficial fluid velocity u_f to the floating velocity of an average particle u_t, whose calculation is shown in (14)

$$Re_t^2 = \frac{4}{3} \cdot \frac{Ar}{C_D} \tag{14}$$

where Re_t is the Reynolds number of a particle at terminal velocity, Ar is that particle's Archimedes number and C_D is the drag coefficient which can be taken from Figure 3 when the corresponding

Reynolds number is known. The latter can beused to calculate u_t via (12), with the overall calculation being an iterative approximation.

In the progress of the entrainment of solids, particles are continuously moved to the top and if they are replaced by new particles at the bottom, this results in continuous lifting work having to be done by the fluid, thus an increase of the back pressure through the bed is the result, as shown in Figure 2.

2.3 Residence Time Distributions and Reactor Characteristics

As RTD measurements are the central activities of this thesis, the basics on RTD functions as well as the characteristics of idealized and real reactors are to be given here as far as relevant for the thesis. The reason to bother about residence times of particles in the fluidized bed reactor in the first place is that excessively short or long residence times reduce the efficiency of the reaction to take place in that reactor [26], with sub optimal reaction times resulting in flushing of less than optimally reacted particles, whereas super optimal residence times lead to depleted reactants occupying reactor space where fresh reactant could be instead.

Furthermore, irrespective of the actual result, the RTDs measured in a reactor are a source of invaluable information on the kind of mixing that occurred in the reactor under the specific conditions the measurement was made with [26], thus enabling the detection and specific counteracting of problems.

2.3.1 The Residence Time Distribution (RTD)

Following the definition given by H. S. Fogler [26], the residence time distribution $E(t)$ gives the relative amount of tracer material detected in a time interval Δt, starting at a time point t after the time point of injection t_0, hence this function can be called a *differential* RTD. It is acquired from normalizing the measured concentration curve over time $C(t)$ by the total amount of tracer material N_0 injected, as reflected by (15).

$$E(t) = \frac{C(t)}{N_0} \tag{15}$$

Prior knowledge of N_0 is not critical, since it can be acquired from integrating $C(t)$ over the whole time range where the signal is non-zero: $\int_0^\infty C(t)\ dt$.

From this normalized RTD, which is shown in Figure 4, the first momentum $\bar{t}$ can be calculated using (16).

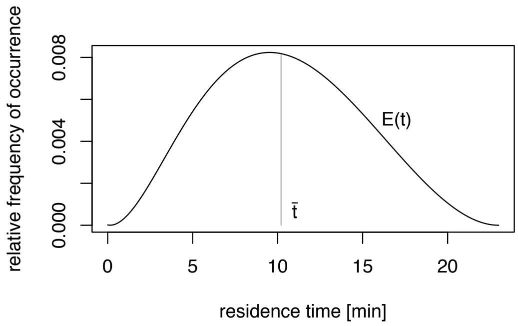

Figure 4: Differential RTD with $\bar{t}$ being the first momentum of the distribution, calculated according to (16).

$$\bar{t} = \int_{-\infty}^{\infty} t \cdot E(t) dt \tag{16}$$

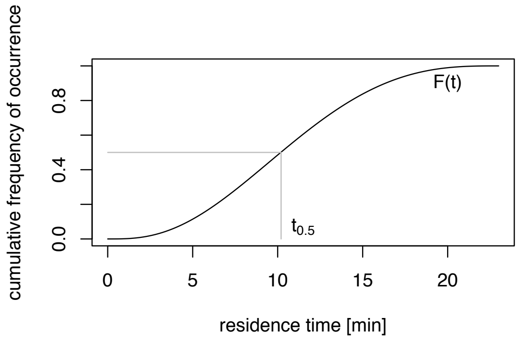

Figure 5: Cumulative RTD with the median residence time being read from the horizontal position of the intersection of the cumulative function with the vertical position of 0.5 of the total amount of tracer material (having lower and equally higher residence times).

As with any differential distribution, another essential concept regarding RTDs is the cumulative or *integral* residence time distribution $F(t)$, which is acquired from integrating up $E(t)$ as defined in (17).

$$F(t) = \int_0^t E(t)\, dt \tag{17}$$

The ultimate use for this transformation is the acquisition of the median residence time, which is as trivial as finding the time point, where the cumulative frequency of occurrence is equal to 0.5, as shown in Figure 5.

The aforementioned applies to the pulse injection method, where tracer material is injected into the reactor entry in a narrow pulse that changes its shape due to a number of effects, the most prominent of which are to be presented here, with some being also shown in Figure 6 and discussed in the subsequent subsections:

(1) Dead times in an ideal plug flow reactor (PFR) cause delays quantified by τ_{PFR}, but no changes in the shape of the peak

(2) Axial dispersion in non-ideal PFRs lead to a widening of the output peak, with the exact shape of the outcome being dependent on the kind of flow that is happening in the reactor.

(3) Ideal continuously stirred tank reactor (CSTR)-like elements (immediate perfect mixing) will cause pulse injected tracers to pass the output with maximum concentration immediately upon entering the reactor volume, then decaying exponentially.

(4) Non-ideal mixing in CSTRs causes a widening of the peak, resulting in a smooth rise and minor changes in the shape of the decay.

(5) Series of ideal or non-ideal reactors of different and/or same type (e.g. measurement at the tubular inlet and outlet of a CSTR will lead to PFR-like behavior of the tubular sections with a CSTR in between) change the shape of the peak in several ways that lead to the final RTD.

Alternatively, there is the possibility to do a step injection, meaning tracer material is constantly fed at a defined and constant rate from t_0 until the tracer concentration in the output reaches that of the injection is to be mentioned. The resulting $C(t)$ curve at the output of the reactor is then somewhat similar in shape to what is shown in Figure 5, however due to high demand of tracer material and lack of advantages with respect to the acquisition of information, the use of this method was refrained from, hence further explanation is omitted.

2.3.2 The Idealized Plug Flow Reactor (PFR)

As examples for ideal reactors there should first be mentioned the plug flow reactor (PFR), a continuous reactor which the reactants flow through without any axial mixing, hence every single particle has the same residence time within the PFR [26]. In such a reactor, the shape of the RTD curve measured at the output of the reactor exactly matches the one at the input, except the output will be delayed by the residence time τ_{PFR}, following the volumetric equation for the estimation of mean residence times τ (18),

$$\tau = \frac{V}{\dot{V}} \tag{18}$$

with V being the total reactor volume and $\dot{V}$ being the volumetric flow into as well as out of the reactor [26].

An illustration of the input and output curves of an idealized PFR as well as a PFR featuring bidirectionally uniform axial dispersion is shown in Figure 6a.

2.3.3 Continuously Stirred Tank Reactor (CSTR)

A second important reactor model is the continuously stirred tank reactor (CSTR), where ideal mixing occurs directly upon the entering of new reactant into the bulk volume, with some particles leaving the reactor almost immediately via the continuously drawn output stream and others staying in the reactor for a very long time, since there is never a total discharge of the contained volume. Still, many of the particles will leave the reactor close to the mean residence time τ_{CSTR}, which can be estimated for ideal CSTRs according to (18). The shape of the RTD of a series of an idealized PFR and an idealized CSTR is described by (19). It is easily transformed into that of an ideal CSTR by setting $\tau_{PFR}= 0$.

$$E(t) = \frac{e^{-(t-\tau_{PFR})/\tau_{CSTR}}}{\tau_{CSTR}} \tag{19}$$

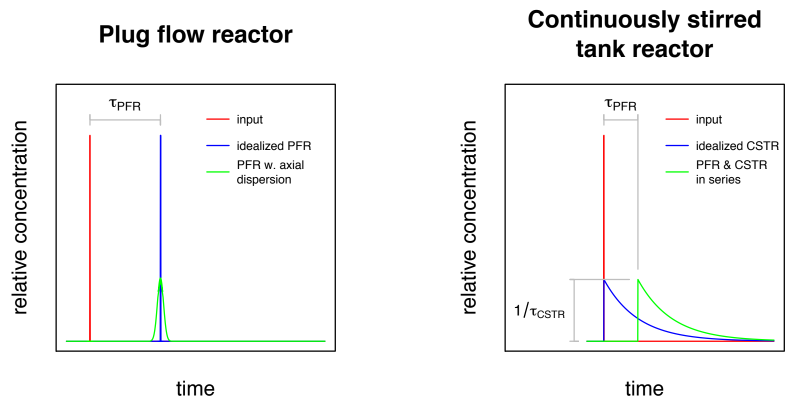

(a) (b)

Figure 6: RTD outcomes of idealized and axially dispersive PFRs (a) as well as that of idealized CSTRs and of a series of an idealized PFR and an idealized CSTR (b) with indication of the characteristic parameters as provided by H. S. Fogler [26].

The idealized input and output curves of an idealized CSTR as well as that of a series of an idealized PFR and CSTR are shown in Figure 6b.

Further deviations from ideal reactors are indicated in Figure 7, considering problems with the reactor design as well as with the choice and flow of the fluid and the tracer material.

As shown by Yagi and Kunii [14], fluidized beds do mostly behave like CSTRs, however since inductive measurement of the kind that was carried out in this thesis obligatorily includes some content of material flow through the inlet and outlet pipes, a mixed model might be the most appropriate for the interpretation of the measured RTD data.

2.4 Inductive Measurement Principles

As from the previous section it is now clear what kind of data there was to be acquired in this thesis, namely a time dependent tracer particle concentration $C(t)$, this section will provide the basic knowledge on *how* this data could theoretically be acquired.

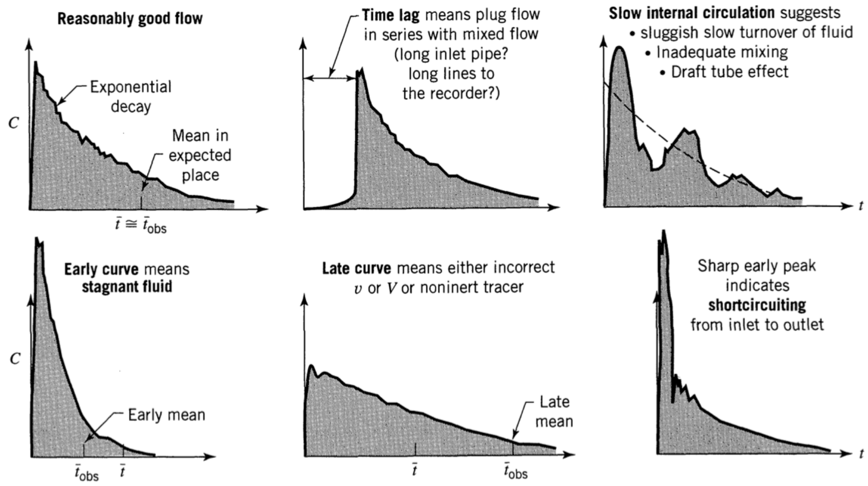

Figure 7: Problems of real mixed-type reactors and their causes, taken from O. Levenspiel [27].

2.4.1 Static Electromagnetism

Prior to the explanation of the electrodynamical phenomenon of induction, the relation of the static flow of electrical current and thereby established magnetic fields according to Ampère's Law is to be stated: When current is flowing upwards through a vertical conductor (noted in traditional flow direction, opposite to the direction of the electrons' actual movement), then a circular magnetic field is established with the fields direction being counter clockwise when viewed from above. This field is basically static for as long as the current flow is, with its density being proportional to the amperage and inversely proportional to the distance normal to the conductor [28]. The circular field created around a single wire can be transformed into a somewhat linearly directed shape by wrapping that wire into a coil as illustrated by Figure 8. Despite the fact that electric fields and electromotive forces do occur in vicinity to resting conductors flown through by constant current, as stressed by Assis et al. [29], these effects are of marginal importance and will be neglected in this thesis.

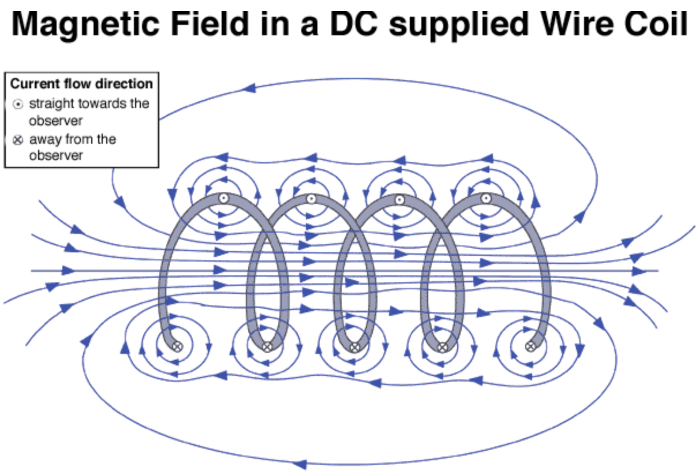

Figure 8: Magnetic field lines run circularly around each wire in direction of a right handed thread and interfere to form a linear field in the center of the coil.

2.4.2 Electromagnetic Induction

The phenomenon of induction can be described as the following in accordance to Henry's Law: when an electric conductor is located in a magnetic field, then movement of the conductor relative to the magnetic field or other forms of changes of the magnetic field at the position of the conductor will induce an electromotive force, hence electric current flow in that conductor, especially if that conductor has a closed circuit outside of the magnetic field. This induced current flow leads to the establishment of a secondary magnetic field, following the description in section *2.4.1*. According to Lenz' Law, the direction of the induced current is always such as that the secondary magnetic field will be directed exactly opposite to the direction of the change in magnetic field that induced the current in the first place [28].

As a consequence, if a current carrying conductor is resting in a static magnetic field (whose origin can be either external or even the result of current flow through the conductor itself), then any change in current is accompanied by the establishment of a secondary magnetic field, whose establishment induces a secondary current that again opposes the direction of change in primary current, meaning a rising current will be choked by the inductive effect, while a decaying current will be enforced. This is why electromagnetic induction is said to add inertia to a current flow.

2.4.3 Inductive Measurement of Ferromagnetic Tracer Particles

Now, if a conducting particle is located within a coil, then induction will not occur unless that particle is moved or the current flow in the coil changes. While the particles participating in a circulating fluidized bed are obviously in motion, especially at the locations where the placement of measurement coils is purposeful, measurement of changes in a constant current due to tertiary currents back-induced from the magnetic fields established by currents induced in the moving particles is not viable in practice, since the currents back-induced in the coil are negligible considering the relation of size, velocity and concentration of the particles in the coil.

In practice, high frequency (HF) alternating current (AC) are used, causing considerable induction in the particles by the high rate of change of the magnetic field and therefore back-induction sufficiently high to deflect the frequency or phase of the primary current.

When taking a closer look to HF ACs of sine or square shape flowing through measurement coils, every transition from peak to trough and reverse represents a change in current flow, which causes a magnetic field to be established in one direction for as long as the transition takes, followed by a slight decay of the field when the current is at its maximum or minimum and therefore not changing (much), followed by the destruction of the magnetic field and establishment of a new field in opposite direction at the transition of the current flow towards the other extreme.

As there is a magnetic field constantly established and collapsed, this change in magnetic field leads to the constant induction of a secondary current which, according to Lenz' Law, is directed opposite to that given at the time by the AC-curve. The inertial dynamics of this counter current induction can even be a critical part of the generation of the AC signal in the first place, as shown in section *2.4.4.1*. In other setups, it can also have potential influence on the frequency of an externally generated oscillating signal or can cause potential phase-shift to such a signal.

When metallic material is introduced to the constantly changing magnetic field, this material alters the magnetic permeability μ of the field's surrounding and thereby the inductivity of the measurement coil, as quantified by (20), due to one or both of the following effects:

Firstly, any electrically conducting object will induce so called eddy currents [17], which in turn establish a small secondary magnetic field [30] that interferes to a small extent with the primary magnetic field and therefore with the induction of a secondary current in the coil, which influences the overall frequency of the AC signal.

Secondly, ferromagnetic particles as a consequence of their magnetic properties also interfere directly with the magnetic field. Instead of favoring the dispersion of the field by instantly shorting the eddy currents created across features of their geometry, more inertia is added to the existing field since the atoms align their magnetic field to the one they experience from outside.

The different effects of ferrous and non-ferrous metals is also reflected in the signal deflection of the detection system, with the response to ferrous particles being distinctively stronger and opposing the direction of the one observed with non-ferrous materials. However, depending on shape and size of the objects, according to C. W. Moreland [31], eddy current effects of large ferrous objects can also reversely override the ferrous effect.

The inductivity of a single layer coil whose interior is filled with any material can be calculated from the material's magnetic permeability and the coil dimensions by (20) as presented by Sanderson and Lim [16]

$$L = \mu_r \cdot \mu_0 \cdot \frac{N^2 \cdot A}{l} \tag{20}$$

where L is the inductance of the coil in Henries H, μ_0 is the magnetic permeability of vacuum, which happens to be equal to $4\pi \cdot 10^{-7} H/m$, μ_r is the magnetic permeability of the material relative to μ_0, N is the number of turns the coil consists of, A is the cross sectional area of the interior of the coil and l is the length of the cylinder described by the coil.

They also provide a table of μ_r values for various ferromagnetic materials, which range from very close to 1 (magnetite powder), via some around 100 (Iron, Nickel, Cobalt) up to 20000 (Ferrites), with ferrites being oxides of various transition metals and Iron, e.g. $MnZnFe_2O_4$ [16].

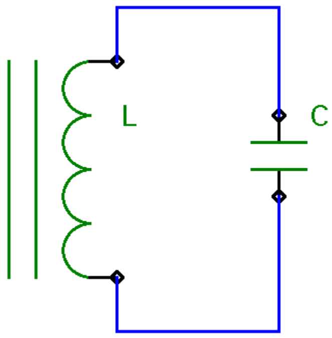

Figure 9: Tank circuit as an electrical resonator.

2.4.4 Principles of Beat Frequency Oscillation (BFO)

As the previous sections focused on the physical basis that enable inductive measurement of ferromagnetic tracer material, this section is there to widen the view and add context as to promote a wholesome understanding of the measurement device presented in section *3.2.1*.

A BFO inductive measurement device basically consists of two separate oscillator circuits, one of which contains the measurement coil that determines the oscillator's output frequency and the other contains some kind of element that makes it adjustable in reference frequency. The signals of both, measurement and reference oscillators are mixed and processed so only the sensitive audible beat frequency remains for further analysis.

As it became clear from the previous section that a HF AC source is necessary for such kinds of measurements, the essence and working principle of an oscillator is to be given in the following section:

2.4.4.1 Principles of Electric Oscillatior Circuitry

An oscillator is an electric circuit capable of producing an AC signal from a direct current (DC) voltage. Its central element is typically at least one resonant or tank circuit, which in its most elementary case is made up by an inductor and a capacitor connected in parallel, as shown in Figure 9.

The principle of operation of such a tank circuit is a constant conversion of energy between the forms of capacitor charge, current flow and a thereby established magnetic field. With the excitation of such a system - e.g. the complete charge of the capacitor without any external current flow - the cycle of oscillation will begin as the capacitor equals out its charge by current flow through the inductor. With that flow of current, driven by the discharge of the capacitor, the inductor creates a magnetic field. When the capacitor charge is depleted, the magnetic field begins to decay, inducing a current flow that is equidirectional to that before, causing the capacitor to become charged reversely compared to the initial state. When the magnetic field is depleted, the capacitor is fully charged in the reverse direction so the flow of current, establishment and collapse of the magnetic field and recharching of the capacitor will proceed as described in reverse direction, by which the cycle is closed and will be repeated.

Under idealized conditions such as zero resistance in the components and their connections and no interference with any measurement circuitry or the environment, this excited tank circuit would oscillate by itself without decay in amplitude. The rate at which the oscillation takes place is called the circuit's resonant frequency, which can be calculated according to (21), that also holds for some non-ideal oscillators such as the Clapp oscillator [31, 32]

$$f = \frac{1}{2\pi \cdot \sqrt{L \cdot C}} \tag{21}$$

with f being the resonant frequency in Hz, π being the circular geometry constant needed for conversion from rad to Hz, L being the inductance of the inductor in H and C being the capacitance of the capacitor F.

However, as losses are inevitable, well balanced feed back amplification of the oscillating signal is needed to satisfy the Barkhausen criteria for the establishment and maintenance of such an oscillating signal, which state that the ratios of signal amplification and decay must be greater than unity for the establishment of an oscillating signal and be exactly at unity for its maintenance [32].

2.4.4.2 The Beat Effect

As the change in inductivity of a coil compared to its total inductance is marginal when small portions of tracer material are brought to or removed from within the coil, differential measurement has to

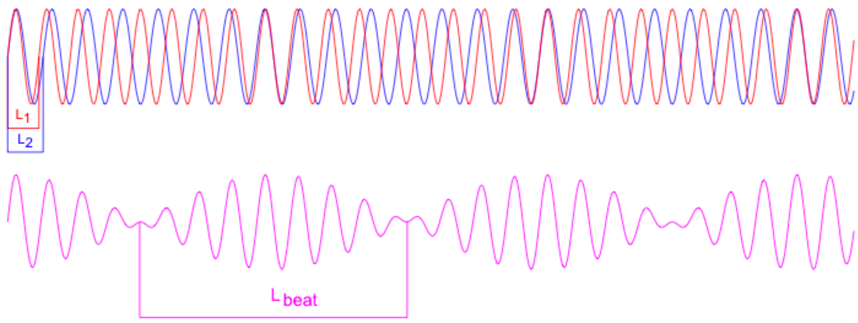

Figure 10: When two continuous sine waves with relatively short primary wave lengths L_1 and L_2 that differ only by a small fraction of their length are added, then a secondary beat wave with a relatively long wavelength L_{beat} results.

be performed in order to enable their detection. With the inductance having effective influence on the oscillation frequency, differential frequency quantification can be done using the phenomenon of the beat effect, which is illustrated in Figure 10. This effect appears most obviously when two sinusoidal waves of relatively high primary frequencies with a very slight difference in frequency are added to each other, as it happens naturally with sound waves in the air or with AC voltages when their wires are connected. Then their sum wave modulates the original frequency in a secondary sinusoidal wave whose frequency is equal to the difference of the primary frequencies. The secondary wave can be isolated by rectification and low pass filtering [31].

3 Experimental Setup

In this section, the used particles, the inductive measurement device, the specifications and positioning of the measurement coils and data processing routines are to be explained in detail as well as the calibration setups and the cold flow model apparatus including the particle loop and the supply of pressurized air.

3.1 Particulate Solids used for the Measurements

The main component of the fluidized beds used in this thesis was made up by glass beads which had a mean d_{SV} of 130 μm with most of the particles being sized 100-200 μm, and almost all of the beads being contained in the range of 80 to 250 μm as a it was indicated by a volume related analysis using a Mastersizer 2000 device by Malvern Instruments (see the output sheet of the analysis in the *Appendix*). The glass had an inner density of 2450 kg/m^3, while the bulk density was 1574 kg/m^3.

As ferromagnetic tracer particles, ferritic stainless steel 1.4742 with nominal diameters of 45-100 μm and an estimated d_{SV} of 80 μm have been used. Accurate analysis of the particle size composition has not been done, however particles smaller than 32 μm had been removed before by sieving. The inner density of this material was 7560 kg/m^3.

The calculated values for u_{mf} were 0.0150 m/s for the glass beads and 0.0176 m/s for the tracer particles. Despite the subtle differences, both kinds of solids were regarded hydrodynamically equivalent.

3.2 Measurement Equipment

3.2.1 Beat Frequency Oscillator

In the course of this thesis, one major emphasis was put on the development of a device capable of converting small changes in inductance of the measurement coils to frequency shifts in an AC output signal.

In the current case the signals of two separate L/C-oscillators (with the inductance parts (L) being a measurement coil for one and a reference coil for the other oscillator and the capacitive parts (C) being exchangeable capacitors) are superimposed to generate a beat, as explained in section *2.4.4.2*. With the measurement of the beat frequency and the detection of its deflection, the device meets the requirements for being called a BFO metal detector. Depending on the circuit design, amplification rate, inductance and capacitance values, the wave lengths of the individual oscillators can be set to practically useful values ranging from below 100 kHz to beyond the measurement capacities of the oscillator that was available in the lab, but it was believed to be in the MHz-region.

As the deflection of the inductivity of the measurement coils has a multiplicative effect on the individual oscillator's frequency (see (21), the beat frequency is deflected more vigorously when the individual frequencies are higher given the same change in inductivity [31]. Hence, the primary frequencies have to be high enough for the device to provide sufficient sensitivity for the measurement of low amounts of tracer material. However, when the frequencies are chosen too high, stability of the signal can become a problem, which was observed and treated as follows, as a result of both, recommendations by C. W. Moreland [31] and practical experiences made during the development of the device:

(1) The distance between the individual wires of a coil, including the start and end pieces, has substantial influence on the total inductivity of the coil. Therefore, any wire wound to a coil that is taking part in the circuit were fixed using hot glue or at least duct tape and the end pieces were packed into solid joints ending in compact, non-compressible cables.

(2) Changing magnetic fields in the environment such as electric motors or power transformers were kept at distance as far as possible, as their magnetic fields were observed to potentially suppress the beat signal partially or even completely, but even if it interfered just slightly with the beat signal, the compatibility of the signal with its further processing was suffering severely. Also, with the simultaneous operation of more than 1 measurement positions, the lightheaded decision to pack all oscillator circuits into a single housing resulted in some bleeding, interference and even deflection between the channels. Mounting a metal plate in between the circuit boards and reference coils of each channel helped to minimize the bleed, however any measurements regarding this thesis were performed using only one channel.

(3) Parasitic capacitances between the windings of a coil responded to changes in permittivity in its immediate surrounding when sensitivity was high, resulting in moderate signal deflection when the coil was touched or approached with fingers. Therefore the coil holders for the reference coils were designed and placed such that the coil itself was located centrally in the housing.

(4) Since temperature has some effect on capacitance and inductance values as well as resistance of semiconductors, temperature drifts can lead to signal drift as well, however this was not found to be a major problem during the measurements carried out in the course of this thesis.

Thus, after the available means of stability control have been exploited, a compromise in primary oscillator frequency had to be found that was high enough to provide sufficient sensitivity, but low enough to ensure reasonable stability.

For the adjustment of the primary oscillator frequencies, values of L and C can theoretically be chosen freely as long as the wanted frequency is produced by satisfying (21). However, as the full working oscillator circuit also features portioning, amplification and especially phase adjustment of the feedback signal, which needs to be dimensioned to suit a certain range of L and C values [33], there were also practical limitations. Still, with the frequency determining elements consisting of one coil and two capacitors for each of the oscillators (see Figure 11 for reference), by using different combinations of the capacitance values, the range of practically achievable frequencies included many orders of magnitude even without changing any component between the transistor Q3 and the speaker in the schematic in Figure 11 and was not a limitation to the practical use of the device.

As capacitors are cheap and easily available in a huge range of values, they are predestined as a means for selecting the order of magnitude of the tuning frequency. For fine tuning however, the availability of variable capacitors is restricted to capacitance values in the pF range, which was clearly beyond the scope of values capable of producing oscillation in this setup. This also holds true for varactor diodes which would otherwise have the advantage of its capacitance being controllable by a bias voltage [32].

So, to be able to fine-tune a reference oscillator circuit and therefore produce a meaningful beat frequency, reference coils with movable ferrite cores had to be made, which was possible to do with a reasonable effort (a detailed explanation is given in section *3.2.3*).

3.2.1.1 Design of the Circuitry and Device

The electric oscillator circuit used in this thesis was based on a circuit designed for a metal detector for hobbyist treasure hunting by D. Smith [34]. As the circuit posted on his site provided a solid foundation, the need for development was limited to the following:

(1) Increase the flexibility of the frequency range by making those capacitors exchangeable that directly participate in the resonator and are therefore counted to the frequency determining components.

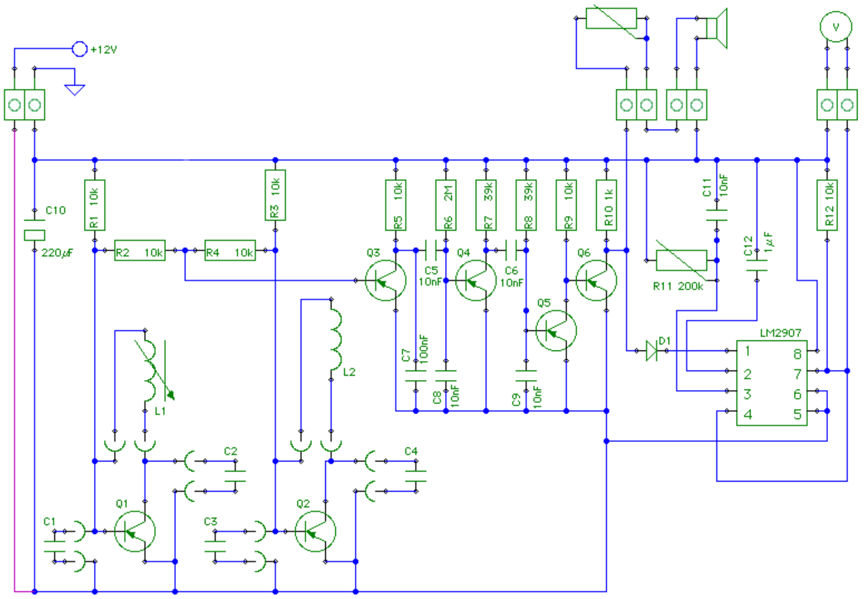

Figure 11: BFO circuit with some parts being specific to the reference oscillator (L1, C1-2, Q1), some to the measurement oscillator (L2, C3-4, Q2), R2 and R4 making up the signal mixer, the central region (Q3-6, R5-10, C5-9) accounting for amplification and shaping of the output signal plus portioning and phase adjustment of the feedback signal and the rightmost region being a measurement transformer that converts the output frequency to a DC voltage.

(2) Adaption of the measurement coil to the shape and needs of the tracer detection in particle removal and return pipes and maintaining the coil's compatibility with a Lock-In Amplifier device developed in parallel by Hofer et al. [35].

(3) Finding a suitable way of signal processing that yields a numerical value which can be logged over time.

(4) Finding layouts for the circuit boards and integrating them into a housing.

The final circuit is depicted in Figure 11, with any non designated components being optional and any components with missing values being exchangeable for the purpose of tuning the oscillators. All the Transistors were of type MPS 751, all the non-electrolytic capacitors were of metal foil type.

The schematic in Figure 11 features several regions:

The reference coil L1, capacitors C1 and C2 as well as the resistor R1 and the transistor Q1 can be assigned specifically to the reference oscillator, while the measurement coil L2 together with the capacitors C3 and C4, the resistor R3 and the transistor Q2 are specifically part of the measurement oscillator.

The resistors R2 and R4 form a tapped voltage divider between the two oscillators and serve the purpose of mixing the two primary signals to generate the beat signal that is then amplified, phase adjusted and shaped by the components R5-10, C5-9 and Q3-6 into a square wave that switches values between 0 and approximately 10 V.

The integrated circuit chip LM2907 and its peripheric components (bias adjustment resistor R11 and output pulldown resistor R12, bypass capacitor C11 and charge pump buffer capacitor C12) work as a measurement transmitter that converts the beat frequency to a DC voltage between 0..10 V. However the sensitivity of the output voltage signal was rather poor and the ripple noise most of the time exceeded the actual signal. By adding a passive low pass in form of bypass capacitors between the voltage output and ground, ripple noise could be reduced, but the overall voltage was raised, significantly reducing the headroom and thereby the measurement range. Due to these difficulties, the measurement was performed by recording the audible beat signal using a standard PC sound card at a sample rate of 48000 Hz and evaluation of the recorded file by software as explained in detail in section *3.2.1.2*.

The 12 V DC power supply shown at the top left in Figure 11 is buffered by the capacitor C10 to prevent oscillations between the power and ground poles.

3.2.1.2 Data Recording and Processing Procedure

As described above and depicted in Figure 12, the primary output of the BFO measurement device was a spike-shaped voltage wave in the audible frequency range with changes of the inductivity of the measurement coil being converted to shifts in the output frequency. After failed attempts to perform on-line conversion of the frequency shifts to DC-voltage shifts, it was decided to record the primary beat frequency signal via a standard PC sound card and to perform the conversion offline by software. The software used for recording the audio files was Audacity 2.0.5, the data processing was then

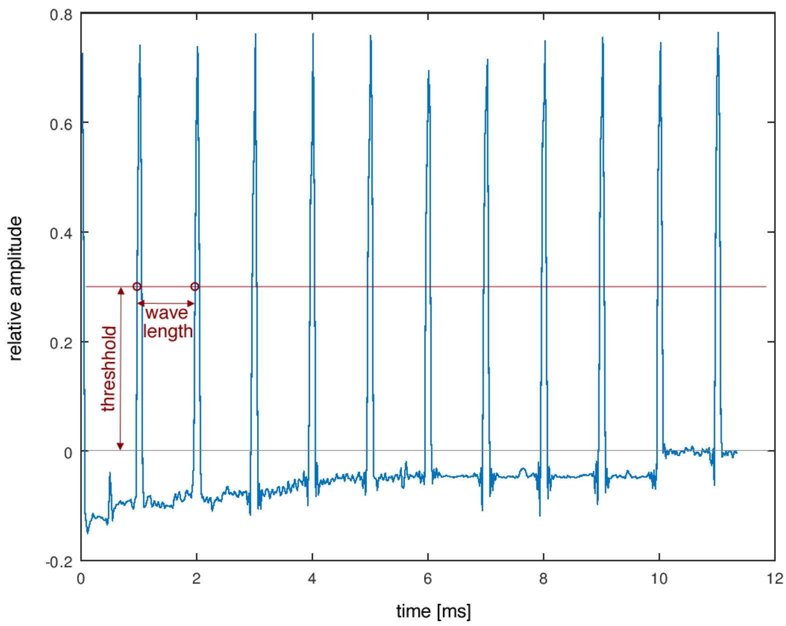

Figure 12: A small snippet of wave data read from the recorded file with points marked where one sample is below and the next sample is at or above a certain threshhold.

performed by a routine written for Octave 4.4.0.

The functionally relevant parts of this routine are presented in Listing 1, with the lines for file handling and function definition purposes being omitted. In the routine, the waveform data from the recorded sound file is first read in, storing the amplitude value of each sample in an array y and providing the sampling rate fs. Then, besides initiating cycle number and start sample number, a threshhold is defined, which, if deceeded by one sample and reached or exceeded by the next, marks the end of one and the beginning of the next wave cycle. The number of samples contained within one wave cycle divided by the sample rate was regarded the wave length of that cycle. The reciprocal of the wave lengths (corresponding to the frequency) are logged into a new array as were the time points (absolute number of the sample a given cycle began with, devided by the sample rate). As some artifacts were encountered where the threshhold was crossed during one wave cycle, resulting in outliers with multiples of the base line frequency, a basic smoothening algorithm had been included. To detect such an outlier, a criterion was defined as one wave cycle having more than double the frequency of the highest one of its adjacent wave cycles. If the algorithm was enabled and the criterium was met, the smoothing was done by assigning the mean value of the frequencies of the adjacent wave cycles before and after the outlier to the cycle in question. This was obviously not an exact solution, as either the wavelength before or after the artifact was also affected by the artifact, besides the criterion was leaving much room for not detecting potential outliers. However, as the data featured some very far outliers, it probably did benefit more than it suffered from using it.

Listing 1: Arrangement of functionally relevant code that was used to quantify the frequency of each wave cycle from waveform data

```
% read in the waveform from .wav file(s)
[y, fs] = wavread(filename);

% initiate the cycle number with 0 and start sample number with 1
cycle=0;
cycleStartSamp = 1;
threshhold = 0.3;

% loop over all samples except the first and last 10
for(nSamp = 10:(length(y)-10))

  % store adjacent sample values
  currSamp = y(nSamp);
  nextSamp = y(nSamp+1);
  % check if the threshhold is being exceeded between the two adjacent samples
  if(currSamp < threshhold & nextSamp >= threshhold)

  % in the first cycle, store sample number and set cycle number to 1
    if(cycle==0)
      cycleStartSamp = nSamp;
      cycle = 1;
    else

    % for all other cycles, store frequency and time stamp of that cycle
      cycleLength = nSamp-cycleStartSamp;
```

```
      waveLength = cycleLength/fs;
      freq(cycle)= 1/waveLength;
      t(cycle) = nSamp/fs;
      cycleStartSamp=nSamp;

       % In case that suspiciously short wave cycle artifacts have been encountered, a smoothing algorithm has been included
       if(smoothing>0)
          % If one cycle was much shorter than both the cycles before and after, then force the artifact cycle to be the mean value of the two adjacent cycles
          if(freq(cycle-1)>2*max(freq(cycle), freq(cycle-2)))
            freq(cycle-1) = mean(freq(cycle-2), freq(cycle));

          endif
        endif
        cycle +=1;
      endif
    endif
  endfor
```

3.2.2 Measurement Coils

The cold flow model used in this thesis was equipped with measurement coils at the solids removal and return pipes at the positions highlighted in Figure 17. Those coils had an inner diameter of 60 mm, a cylinder length of 12 mm, as shown in Figure 13. Multiple layers of 0.35 mm enamelled wire were wound onto 3D-printed coil holders as densely as possible with the help of a lathe. The produced coils were measured to have an inductance of 8.1 mH, using a Voltcraft LCR-9063 measurement device which operates at frequency of 266.6 Hz.

3.2.3 Reference Coils

The reference coils used for fine tuning the reference oscillator were made of 0.15 mm gauge enameled copper wire wound around 3D-printed coil holders in 175 turns. They had an inner diameter of 14 mm and a cylinder length of 10 mm, as depicted in Figure 14. The coil holder was hollow, containing a ferrite core which was moveable in axial direction by means of a threaded pole that extended through a hole in the housing of the device, enabling its operation by an external knob. The inductivity was measured to vary from 146

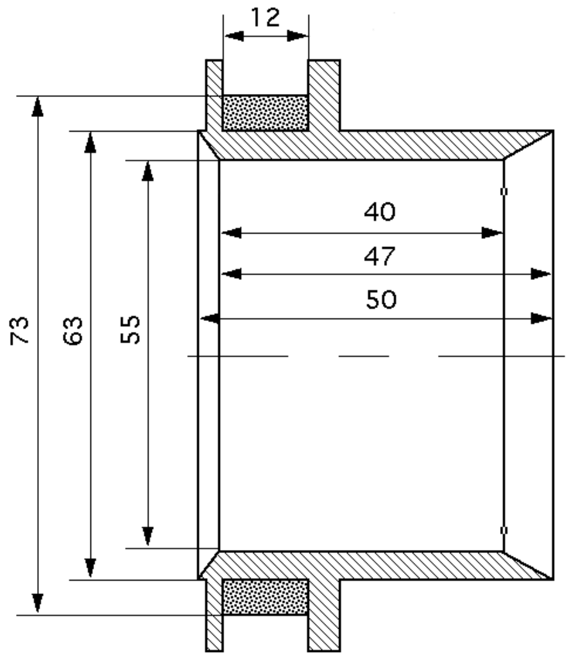

Figure 13: The 3D-printed coil holder containing the coil in the groove between the two external rings.

to 390 mH throughout the range of possible axial positions of the ferrite core using a Voltcraft LCR-9063 measurement device which operates at frequency of 266.6 Hz.

3.3 Calibration of the Measurement System

For the sensitivity testing and calibration of the signal deflection of the measurement device, portions of tracer particles were weighed and added to a bed of fresh, tracerless glass beads in a glass vessel. After mixing with a manual stirrer, each measurement run was started by recording a few seconds of the beat wave signal of the empty coil. Then, the vessel was placed in the center of the coil, left there for a few seconds before removing it again to record a final few seconds of empty signal and stopping the recording. In such a way, the base lines before and after the actual measurements could be averaged over, thus eliminating potential signal drifts that could

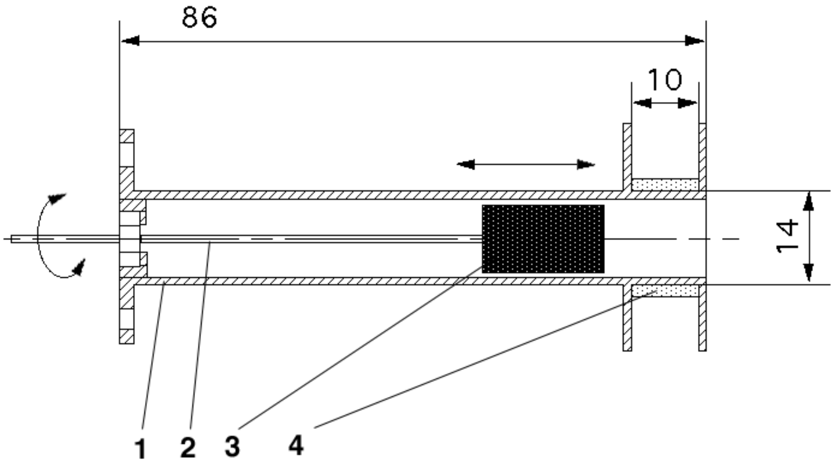

Figure 14: Reference coil assembly including the coil holder (1), a threaded pole (2) that moves the ferrite core (3) into or out of the coil interior (4).

have occurred during the recording. The frequency difference between the average base line and the tracer deflected measurement was regarded the signal deflection of that run.

Any model fitting and evaluation activity was done using R 3.2.1 and RStudio 1.1.419.

3.4 Small Scale Fluidization Pipe

For the acquisition of u_{mf} and u_{mb} of the particles given in section *3.1* and for a series of bed expansion measurements, a desktop scale fluidization chamber in form of a push fitting assembly of an inner PVC pipe and an outer acrylic glass tube was used as shown in Figure 15. Its inner diameter was 50 *mm* and its empty freeboard height was 925 *mm* from the gas distributor plate to the fabric off-gas filter at the top. The gas distributor was a circular plate of acrylic glass with holes of 1.5 *mm* in diameter being drilled in a rectangular pattern with 5 *mm* interspaces.

Its windbox was supplied with pressurized air from a laboratory compressor, limited to 1 *barg* by a reducing valve and controlled in volumetric flow using a rotameter with a built-in adjustment valve.

The calibration chamber was filled with glass beads to a height of 162 *mm* above the gas distributor, which expanded to 168 *mm*

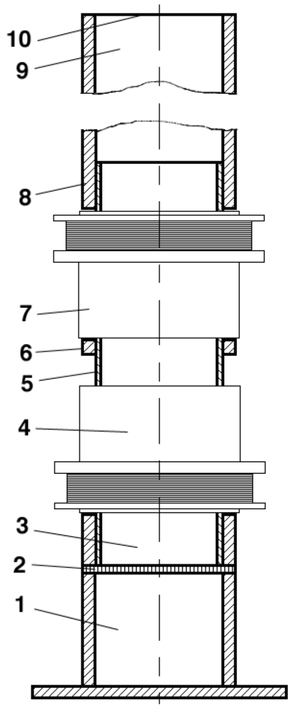

Figure 15: Drawing of the small scale fluidization pipe with its functional features being the windbox (1), gas distributor (2), consisting of a hole drilled acrylic glass plate and a fabric filter attached to its lower surface, fluidization chamber (3) and also depicting the possible measurement arrangements, such as a coil being mounted around the inner PVC pipe (5) either in lower position (4) or higher position (7), in the latter case it was supported by an adjustable acrylic glass ring (6). An outer acrylic glass pipe (8) is mounted on top, containing the upper section of the bed and the freeboard (9), which is limited on top by a fabric off gas filter (10).

when the bed was coming to rest after fluidization.

A measurement coil was mounted in one of the two positions indicated in Figure 15, with the higher position being still well below the bed surface at any fluidization rate.

For the evaluation of u_{mf} and less probably a differing u_{mb}, the regulation valve was fully closed and then slowly opened, until the first movement was visually observed in the bed. After u_{mf} was found, the valve was opened further to evaluate how the visual characteristics of the fluidization would change and what fluidization regimes could be reached. No inductive measurement was performed during the evaluation of the particle and fluidization properties.

For the measurements regarding the bed expansion, a set of fluidization velocities were chosen, ranging from u_{mf} to the maximum that could be measured with the available rotameter. For the actual measurement of the bed expansion at each velocity, the the beat signal was recorded into an audio file starting with the acquisition of the first base frequency when the regulation valve was fully closed. After a few seconds, the valve was opened and manually adjusted to reach the nominal fluidization velocity as closely as possible. The valve was left opened for the duration of around 20 seconds and then fully closed, continuing the measurement for another few seconds to acquire a second base frequency, for the case that signal drifts might occur. The frequency deflection was calculated as the difference between the active frequency while fluidized, averaged over the holding time and the mean value between the frequencies before and after the fluidization. The raw data tables are given in the *Appendix*.

3.5 Design of the Cold Flow Model

For the RTD measurements, a cold flow model with a bubbling fluidized bed was used, with the main chamber dimensions being 200 x 400 mm in footprint, having around 300-400 mm nominal moving bed height and an empty freeboard height of 1890 mm from the gas distributor/base plate to the off gas filter.

The wider side walls were featured with large windows of exchangeable acrylic glass featuring holes for the mounting of model heat exchanger pipes in various combinations of pipe diameter and interstitial distances. However, when measurements were made regarding this thesis, none of those pipes were mounted, but replaced with flat plugs.

The base plate was an aluminum plate of 6 mm thickness featuring a total number of 74 metal sinter filters evenly distributed throughout the basal area. Beneath the bottom plate, the windbox was located, containing a gas inlet pipe in its center that was sealed shut at its end, but featured ventilation slits through the length of the pipe laterally underneath its axis (see Figure 17 for reference). Thereby, homogeneous distribution of the gas flow throughout the openings of the base plate was sought to be put to high fidelity.

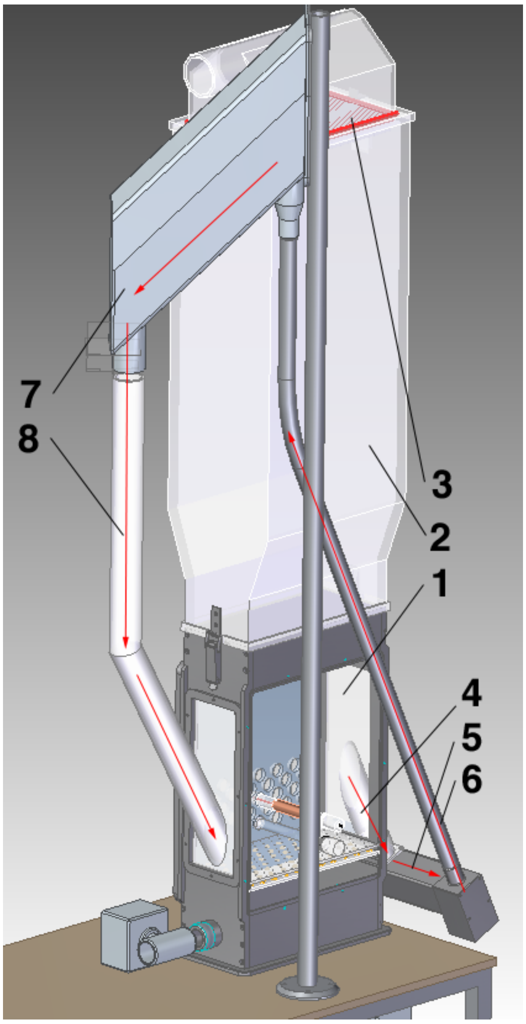

Figure 16: 3D-view of the cold flow model assembly from its rear side, depicting the fluidized bed chamber (1), the freeboard (2), the freeboard's off-gas filter (3), the particle removal pipe (4), the screw conveyor (5), the riser pipe (6), the particle separator (7) and the particle return pipe (8). The direction of movement of the particles in the loop is indicated by red arrows.

3.5.1 The Particle Loop Assembly

At the narrow sides of the fluidization chamber, the particle inlet and outlet pipes were located. Both were acrylic glass tubes mounted

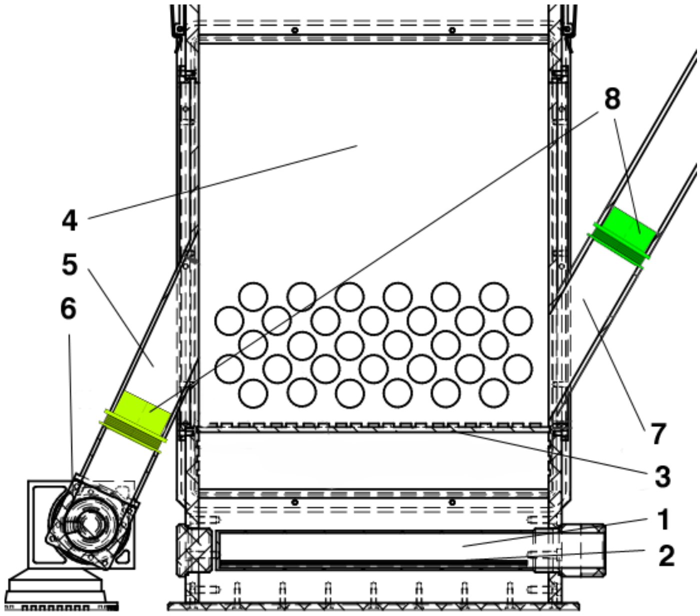

Figure 17: Sketch of the front view of the fluidized bed chamber, showing the dead end gas inlet pipe (1) with its ventilation slits (2) that feed the windbox, whose only exit is the gas distributor plate (3) which provides the primary gas flow for the fluidization chamber (4). All the mounting positions for crossing pipes were sealed with plugs (○). At the particle removal pipe (5), solids exit the fluidization chamber and descend to enter the screw conveyor (6). After passing the particle loop, the solids return to the chamber via the downcomer pipe (7). At both, solids removal and return pipes, measurement coils (8) were mounted.

at the angles of 60°(particle return) and 65°(particle removal) w.r.t. horizontal plane to ensure effective particle transportation within the tubes by the force of gravity. These tubes were connected with the fluidization chamber via elliptical junctions as a consequence of the angled cuts.

While the particle return tube of the downcomer had its lower end of the junction with the fluidization chamber close to the base plate, the lower border of the junction of the particle removal tube was located at a height of 80 mm.

When particles pass the barrier of the outlet from the fluidization chamber, they fall down a short distance through the angled outlet pipe into the perpendicularly arranged screw conveyor, which acts as an air seal to prevent pressurized air from the riser from leaking into the main chamber and also controls the particle flow through the loop, provided its workload is saturated (see section *4.1*). The screw was driven by a pneumatic motor after an electric motor had been identified to cause unacceptable noise in the measurement coil at the particle removal pipe.

After passing the screw conveyor, the particles reach the riser pipe, where air is flowing upwards at a velocity that exceeds u_t by an amount that grants reliable pneumatic transport of the solids up to the particle separator, whose main functional feature is an extension in cross section that lowers the gas velocity as to enable free particle sedimentation. The particle separator is also angled about 45°downwards with the gas stream turning 180°around a narrow plate at its lower end, so the particles contained in the gas are firstly directed downwards and will then hardly make the turn but rather fall down the adjacent solids return pipe. Those particles that make the turn by chance however are fed to the freeboard above the fluidization chamber.

When particles fall down the solids return pipe, they descend to the surface of a fixed bed inside the downcomer pipe, whose level is above the one of the fluidized bed in the chamber, since - apart from a small amount of bleeding of pressurized air - fluidization does not take place and therefore there is no evening out of the level in the pipe with the one in the fluidization chamber.

Now, due to the difference in pressure exerted by the mass of solids that follows the difference in levels of the "fixed" bed in the downcomer compared to the fluidized one in the chamber, the solids contained by the bed in the downcomer descend each time space is temporarily provided in the vicinity of the junction. The result is constant re-feeding of particles into the fluidization chamber.

3.5.2 Pressurized Air Supply

All of the main and peripheral applications using pressurized air were supplied by one large compressor that was designed to provide 6 *barg* of pressurized air at high volumetric flow. All of the devices were controlled in volumetric flow after pressure limiting by reducing valves according to the scheme in Figure 18.

For the fluidization of the bubbling bed, the gas distributor was supplied with a pressure of around 0.7 *barg*, which was sufficient

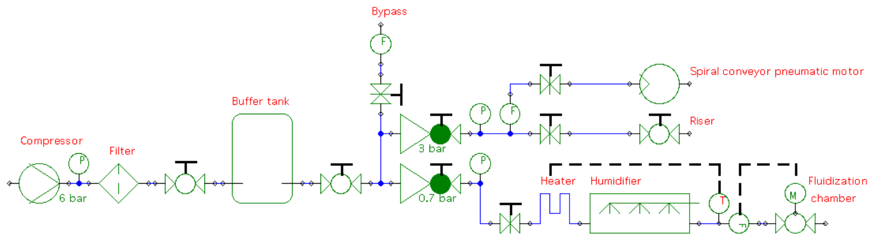

Figure 18: Sketched piping scheme of the pressurized air supply of the cold flow model device, beginning with the compressor in the far left of the Figure, proceeding to the bypass pipe and pressure reducers via filters and the buffer tank. Every branch including the bypass has a manual regulation valve for air flow control with the only exception being the fluidization chamber, where the manual valve is only for opening the branch and the regulation is done by a motorized ball valve.

to produce a volumetric flow of up to 80 Nm^3/h (translating to a maximum fluidization velocity 0.278 m/s in this setup) across the bottom plate, which is the limiting pressure barrier of the system [36].

The riser and the pneumatic motor of the screw conveyor were supplied with a pressure of 3 $barg$. While the first was roughly adjusted in volumetric flow to provide reliable solids transportation but still ensure the stop of entrainment in the particle separator, the latter was visually monitored and manually adjusted in volumetric flow to a range of 8-14 Nm^3/h using a rotameter and a manually operated needle valve.

3.6 Calibration of Particle Circulation Mass Flow

The total mass flow of particles through the particle loop was not inherently quantified by the setup of the cold flow model, hence the particle flow was correlated with the amount of pressurized air supplied to the screw conveyor using the measurement setup and data processing routines presented in the following.

For the measurement of the particle mass flow in the particle loop, a height grid was drawn onto the transparent acrylic glass at the vertical section of the downcomer pipe with a total hight of 500 mm and intersections at every 50 mm. The freeboard assembly was removed to gain access to the junction of the downcomer pipe with the fluidization chamber. This junction was manually blocked while the fluidization and particle circulation were running, so the particles accumulated in the downcomer pipe. The rise of the particle level in the downcomer pipe was filmed at 15 frames per second to acquire each time point when the level reached a marking. After the highest marking had been reached, the junction was unblocked, allowing the level of particles in the downcomer pipe to fall below the lowest marking. As electrostatic effects led to the accumulation of particles in the particle separator that came down in large clogs at unpredictable times, the data was clear to become very noisy. Hence, 6-7 measurement runs were performed at each rate of air supply to the screw conveyor. The main chamber was fluidized with a rate of 20 Nm^3/h to avoid excessive particle spill due to the missing freeboard assembly and the air supply of the screw conveyor was adjusted to 8, 10, 12 and 14 Nm^3/h.

When the time data was acquired for each height value in each measurement run, linear trend lines were fitted to the progression of each run. As it was not clear whether the time when the level reached the grid line zero was over or underestimated due to the clogging noise, the intercept data was omitted and only the slope values were used for the acquisition of a general calibration model. The velocity of the rise of the particle level was converted to mass flow according to (22),

$$\dot{m} = \frac{\Delta h}{\Delta t} \cdot A \cdot \rho_b \tag{22}$$

where $\dot{m}$ is the mass flow of particles in kg/h, Δh difference in particle level in the downcomer pipe in m per time interval Δt, A is the cross sectional area of the internal space of the downcomer pipe in m^2 and ρ_b is the bulk density of the glass particles, as encountered in the downcomer pipe in kg/m^2.

The final calibration model is presented in section *4.1*.

3.7 RTD Measurement Procedure

For each RTD curve measurement run, first the pressurized air supply and PLU were started. Then, the air supply to the fluidization chamber was set to the desired value by an input at the PLU. As soon as the fluidization activity was observed to be constant, the riser and screw conveyor were fed with their respective air supply and controlled to the desired solids circulation rate.

While the bed was fluidized and circulated for some minutes before the tracer injection, the tracer was kept immobile in the downcomer pipe, upstream of the input measurement coil by means of an assembly of strong permanent magnets arranged around the pipe.

Pulse injection of the tracer material was performed by manually removing the magnet assembly as quickly as possible, followed by free fall of the tracer front through the input measurement coil to the semi-fixed bed of the downcomer pipe until it reached the reactor and was gradually eluted through the particle removal pipe.

The magnet assembly was re-attached to the downcomer pipe immediately after the injection to immobilize any tracer particles that pass the particle loop, preventing them from re-entering the chamber.

4 Results & Discussion

4.1 Calibration of the Particles Circulation Rate

The calibration model for the prediction of the particle mass flow through the particle loop based on the volumetric air flow through the pneumatic motor of the screw conveyor is shown in Figure 19.

The data points represent the average slope values of the accumulation of particle mass in the downcomer pipe as acquired in the calibration process described in section *3.6*. The excessive noise was accounted to electrostatic effects that led to the accumulation of particles in the particle separator that came down in larger clogs at unpredictable times, as mentioned in the previously stated section. The parameters of the fitted calibration model and their significance levels are given in Listing 2, showing reasonable reliability of the slope value, but, as expected, considerable uncertainty in the intercept.

Listing 2: R output of the summary of the linear calibration model regarding the particle mass flow through the particle loop.

```
Call:
lm(formula = dataY ~ dataX)

Residuals:
```

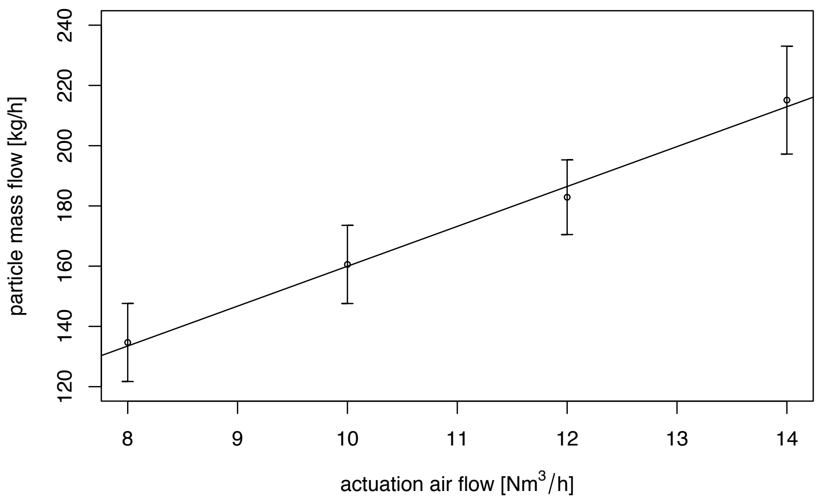

Figure 19: Calibration data of the mass flow of particles in dependency of the volumetric air flow through the pneumatic motor of the screw conveyor. The error bars represent standard deviation.

```
     Min       1Q   Median       3Q      Max
 -22.320   -9.196   -2.078   12.165   31.554

Coefficients:
            Estimate Std. Error t value Pr(>|t|)
(Intercept)   27.574     14.716   1.874   0.0737 .
dataX         13.240      1.281  10.336  4.08e-10 ***
---
Signif. codes:  0  ***  0.001  **  0.01  *  0.05  .  0.1     1

Residual standard error: 13.97 on 23 degrees of freedom
Multiple R-squared:  0.8229, Adjusted R-squared:  0.8152
F-statistic: 106.8 on 1 and 23 DF,  p-value: 4.08e-10
```

4.2 Correlation of the BFO Frequency Deflection to the Relative Content of Steel Powder Within the Coil

The BFO device was calibrated to detect changes in tracer concentrations by means of a correlation factor (slope). The intercept parameter has no particular meaning, as the differential frequency baseline is dependent not only on the individual coil build and the magnetic permittivity of the surrounding, but also on the setting of the reference coil and also signal drifts caused by uncontrolled but influential factors such as temperature.

In this Calibration run, the particle mixes were prepared in a glass vessel which caused distinct signal deflections even before its first contact with ferrite tracers. Similarly, ferrite free glass beads also caused a noticeable signal deflection.

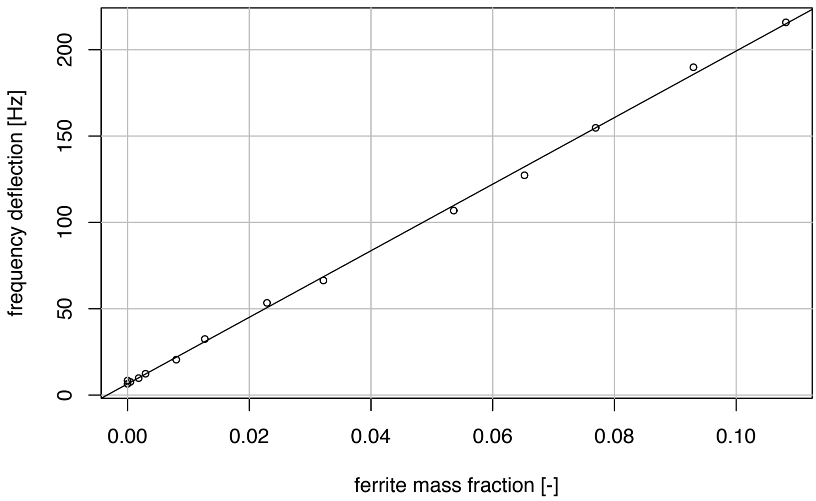

Figure 20: Calibration graph of the BFO device, showing the frequency deflection in dependency of the ferrite content.

The calibration model fit is shown in Figure 20, where no systematic deviations from linearity can be seen, with the uncertainty being reasonably low. In the context of RTD measurements, these features are the most important outcome of the device calibration, as RTD curves are evaluated by their shape and temporal location.

The slightly sinusoidal progression of the deviation of the measurement points from the model was vaguely suspected to resemble oscillating manual mixing habits of the operator, but could just as well have formed purely by chance.

If the correlation factor was highly accurate, reproducible and equally valid for both mounted coils, mass balancing of tracer material might be possible, but was not an objective of this work.

The fit of the linear model was also statistically evaluated, with the R-output being shown in Listing 3, where especially the good R^2 values underline the applicability of the model.

Listing 3: R output summarizing the fit of the linear calibration model to the measured frequency deflection in dependency of the ferrite content of the particle mix within the coil.

```
Call:
lm(formula = BFOcal$DF ~ BFOcal$ferrite)

Residuals:
    Min      1Q  Median      3Q     Max
-4.904  -1.098   0.099   1.329   4.144

Coefficients:
                Estimate Std. Error t value Pr(>|t|)
(Intercept)       6.4859     0.8863   7.318 9.25e-06 ***
BFOcal$ferrite 1927.8070    17.6807 109.035  < 2e-16 ***
---
Signif. codes:  0  ***  0.001  **  0.01  *  0.05  .  0.1     1

Residual standard error: 2.429 on 12 degrees of freedom
Multiple R-squared:   0.999,  Adjusted R-squared:   0.9989
F-statistic: 1.189e+04 on 1 and 12 DF,  p-value: < 2.2e-16
```

4.3 Bed Expansion Measurements

As bubbling fluidization leads to fluctuating bed expansion, also the tracer concentration decreases, either only temporarily with each bubble or constantly but with fluctuations when bubbles are small but numerous. The tracer concentration and its fluctuation were measured in two distinct vertical positions, yielding valuable information on the bubbling behavior of the bed as well as the BFO device's capability to trace it.

Before the actual measurement runs, u_{mf} was determined to coincide with u_{mb} at 0.028 m/s, which was almost two times the calculated value. However, the procedure for determination of u_{mf} described in section *3.4*, as electrostatic and other hysteresis effects may cause fluidization to occur only well above u_{mf}.

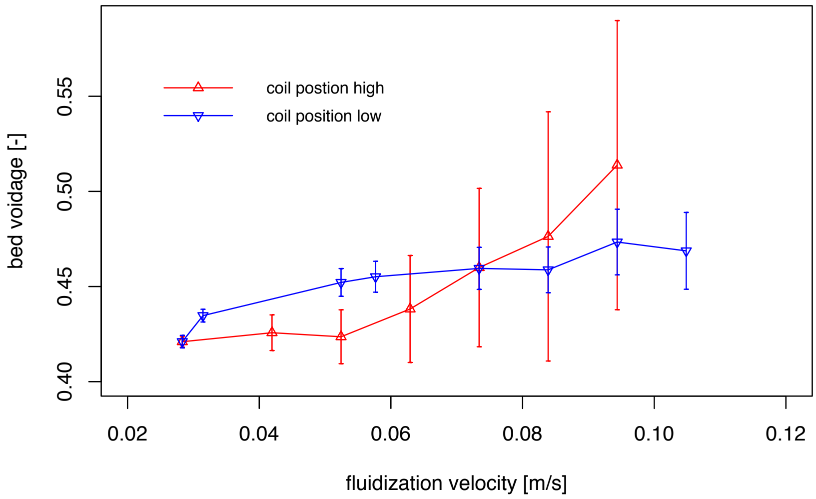

Figure 21: Increase of bed voidage caused by bubbling fluidization at various superficial velocities in both coil positions, low and high. The error bars represent standard deviation.

The mean values and fluctuations of the signal deviation in the measurement runs are shown in context of the fluidization velocity and the coil position in Figure 21. The measurements featuring high coil positioning obviously show highly elevated fluctuations and therefore longer error bars, which can be accounted to the larger bubble size and more vigorous movement of solids in vicinity to the bed surface as compared to regions located deeper in the bed. The fluctuations become increasingly vigorous at higher fluidization velocities. As the fluctuations of the real signal deflection are limited above (the tracer concentration cannot exceed the one encountered in the fixed bed), but not below, the symmetric standard deviation error bars in some cases even deceed zero.

Examples of frequency progressions in the course of the individual measurement runs are given in Figure 22, where the difference in vigorosity of the fluctuations in tracer concentrations between the coil mounting positions becomes even more tangible. Highly elevated bubbling activity and how it meets the upper limitation

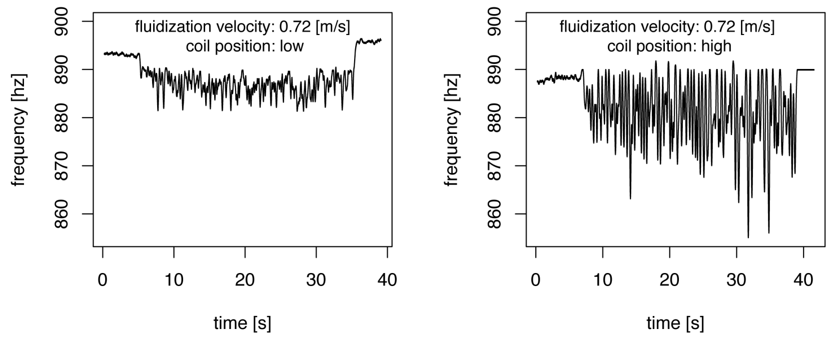

Figure 22: Raw data of exemplary measurement runs for both coil position at the same fluidization velocity, illustrating the differences in bubble size and thereby fluctuation of tracer concentration in the coil.

of the tracer concentration (temporal fixed bed) can be seen in the right graph (coil position: high) compared to left (coil position: low) at the same fluidization velocity.

The interpretation of the exact progression of the mean signal deviations with increasing fluidization velocity at both positions in Figure 21 is not exactly trivial. However, smaller bubble sizes and shallower increase in bed voidage with rising fluidization velocities seems somewhat intuitive for the lower coil position. The sharp increase in average bed voidage in vicinity to the surface also feels natural at higher fluidization velocities. Still, the distinct lag or depression of bed voidage in the higher position at low fluidization velocities is not easily explained.

4.4 RTD Measurements

The raw data acquired form the measurement coil at the inlet of the fluidized bed chamber is plotted in Figure 23. The peak's detailed shape is showcasing the measurement technique's resolution on the time scale and therefore its capabilities for the detection of quick changing conditions, probably suiting for the needs of particularly small fluidization chambers or even for picturing of tracer flows with multiple small (but either only superficial or intrusive) probe heads.

In the graph, one major and a second, minor peak can be clearly distinguished. This shape might most probably have been caused

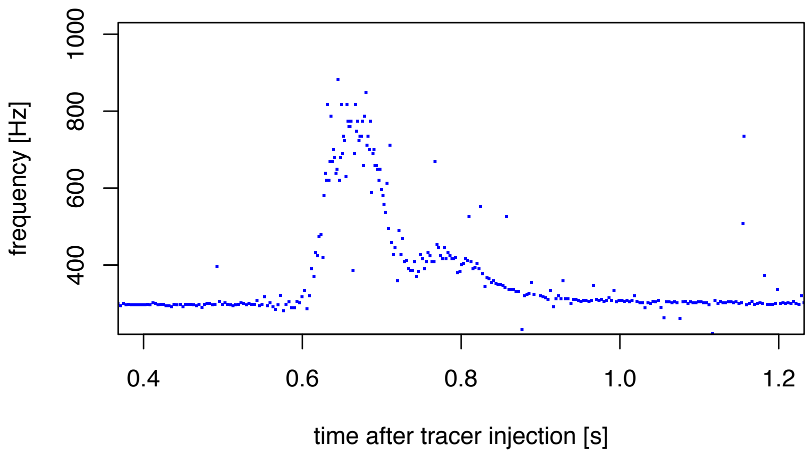

Figure 23: Raw data of the peak measured at the inlet upon the injection of ferritic tracer material.

by the mechanism of the manual tracer injection. The tracer was immobilized by strong permanent magnets held together by two half circular plastic parts and injected by manually parting and removing the parts carrying the magnets, which always stuck at the one end when opening the other. The removal of the still sticking ends was then achieved only with a slight delay, when considerable amounts of tracer material could still have been immobilized at the inner side of the tubing which might have caused the distinct minor peak after the sudden complete removal of the permanent magnets.

Despite its distinct shape, most of the peak extends over less than 0.5 seconds, which is very short compared to the duration of the measurement curve at the outcome (about 3000 s, see also Figure 25) and was therefore regarded infinitely short when evaluating the RTD curve measured at the outlet of the fluidization chamber.

With a maximum signal deflection of almost 500 Hz, this peak exceeds the range covered by the calibration presented in section *4.2* by more than double.

The baseline is distinct and narrow in range, featuring only some outliers - most probably artifacts of the only very rudimental data

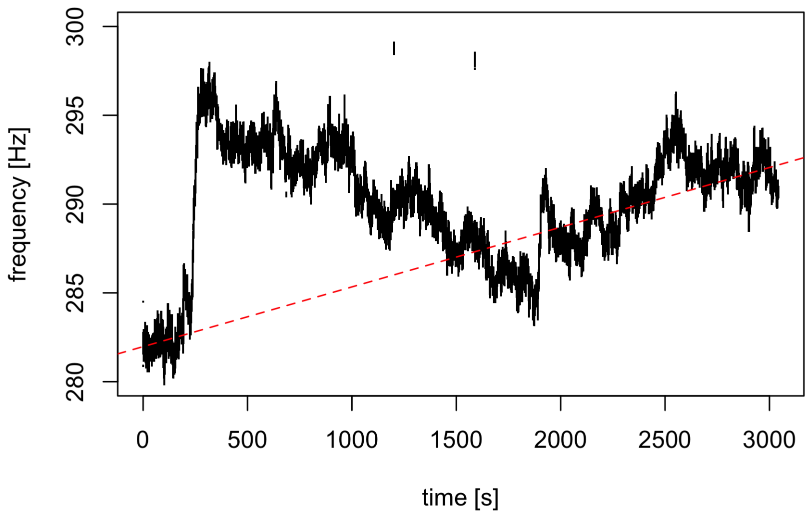

Figure 24: Time dependent concentration of tracer material captured in the course of an RTD measurement run with $u/u_{mf} = 9.26$ and a solids circulation rate of 186 kg/h.

processing routine presented in section *3.2.1.2*.

The raw data of an RTD measurement run captured at the outlet of the fluidization chamber is presented in Figure 24, with a turbulent and non-converging curve shape marking clear deviations from the anticipated result. As the accuracy and reliability of the measurement device was proven in previous subsections, the turbulences of the measured curve was considered a reactor or flow problem (see Figure 7).

The lack of convergence on the other hand was considered a problem of signal drift, which had not been investigated extensively with this device before, but was also encountered with another device when measuring RTDs in the same cold flow model [35].

Due to the lack of viable alternative correction procedures, the signal drift was considered linear and quantified by fitting a linear model through a number of measurement points beforethe peak and where it was believed have ended, similar to the procedure described

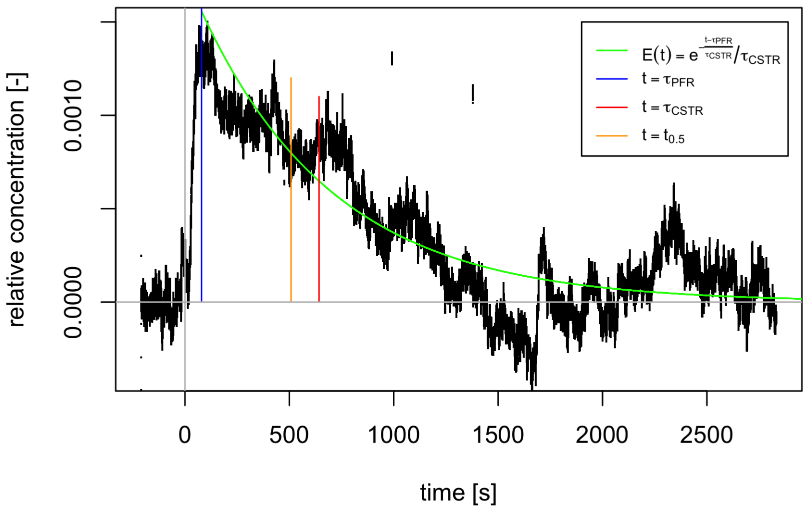

Figure 25: Drift subtracted and transformed E(t) data featuring the median residence time and combined idealized PFR and CSTR model as well as its characteristic parameters. $u/u_{mf} = 9.26$, solids circulation rate: 186 kg/h.

by C. D. Guío Peréz [9] and Hofer et al. [35]. The correction was done by subtracting the value of the linear drift model from each data point at the same time value. Transformation to $E(t)$ was done by deviding every data point of the drift corrected curve by the total area beneath the curve. To the resulting differential RTD a model for a series of an idealized PFR and an idealized CSTR was fit, as shown in Figure 25.

Despite the turbulences including one large signal trough that even becomes negative in a certain range, it can clearly be seen that the declining section of the peak is far more pronounced than its rise. Thereby, and also by the relation of the τ_{PFR} to τ_{CSTR} it can clearly be stated that the measured section of the fluidized bed reactor's CSTR-like features are far more prominent than its PFR-like ones, which is exactly the anticipated outcome considering the cold flow model's only small inlet and outlet piping sections and its large fluidized bed chamber.

The mentioned turbulences might be accounted to inadequate mixing of the solids in the fluidization chamber as a consequence of a too small fluidization velocity or too large (electrostatic) inter particle forces, thus workings in the reactor, as it was indicated originally by O. Levenspiel [27] and as illustrated in Figure 7.

As the model was fit only to the decaying section of the peak starting at $t = \tau_{PFR}$, but τ_{PFR} was actually to be acquired through the procedure of model fitting, the procedure of data augmentation and parameter optimization was repeated in several iteration steps, with the convergence of the parameters being shown in Figure 26. Convergence was apparently reached for both parameters in less than 5 iterations.

The values of the parameters and statistics regarding the final model fit are given in Listing 4, whereas the determination of the mean residence time $t_{0.5}$ of the measurement run is shown in the cumulative RTD in Figure 27.

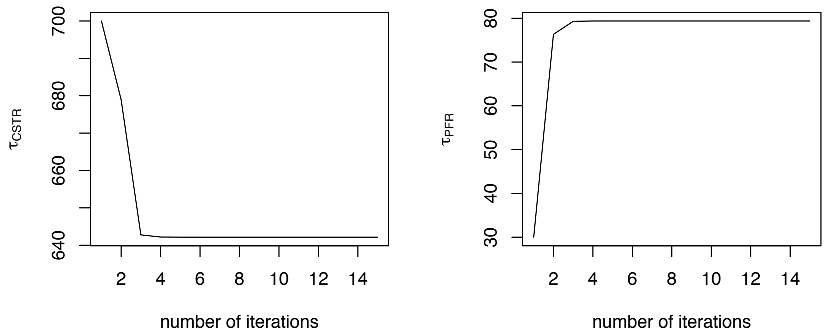

Figure 26: Progression and convergence of the parameters τ_{CSTR} and τ_{PFR} in the progress of the iterative model fitting.

Listing 4: R output summarizing the fit of the delayed exponential model to the tracer concentration measurement curve.

```
Formula: E0 ~ exp(-(t0 - tauPFR)/tauCSTR)/tauCSTR

Parameters:
         Estimate Std. Error t value Pr(>|t|)
tauCSTR 642.1549     0.5486    1170   <2e-16 ***
tauPFR   79.3767     0.3872     205   <2e-16 ***
---
Signif. codes:  0 *** 0.001 ** 0.01 * 0.05 . 0.1   1

Residual standard error: 0.0002019 on 800180 degrees of freedom

Algorithm "port", convergence message: relative convergence (4)
```

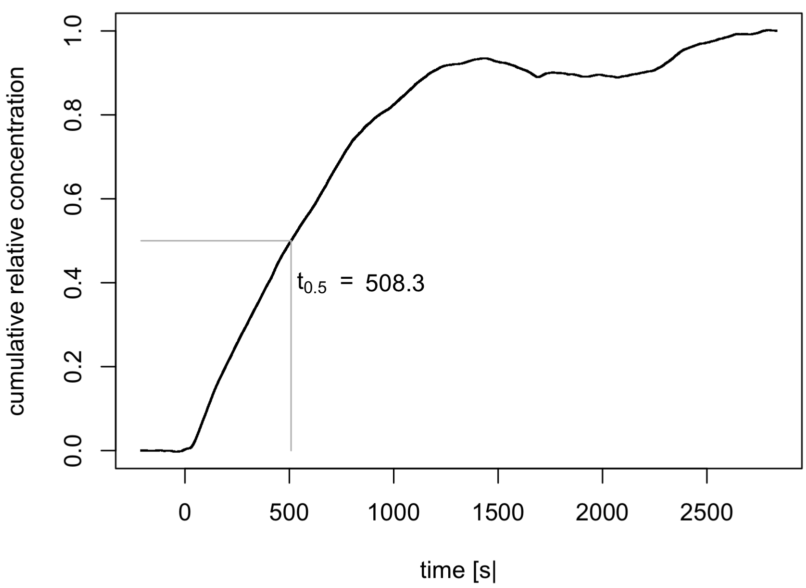

Figure 27: Cumulative RTD.

5 Conclusions & Outlook

It can clearly be summarized that inductive tracer measurements can be achieved at the level of capturing RTDs by means of a simple, low cost and relatively easy to build BFO device in combination with a standard PC and open source software even at pipes of a pilot-scaled cold flow model. Critical requirements thereby are that good care is taken when dimensioning of the frequency determining parts of the oscillators, a robust build of the coils and proper spacing of the oscillator circuits from each other as well as from other sources of fluctuating electric fields.

5.1 Suggestions for the Improvement of the Performance of the BFO Device

Besides the choice of well suited capacitors, the precision of the highly critical fine tuning as well as the stability of the measurement signal depends largely on the mechanical quality of the reference coil, with any small hysteresis potentially having huge non-controllable effects on the signal. Therefore, the build of the reference coils carries a high potential for improving the measurement device, with an improved design possibly including a grease filling of the internal cylinder to reduce the mobility of the ferrite core in response to vibrations.

If the reference coil assembly is less of a problem than assumed, other forms of stability control are to be focused on, namely the quantitative correlation of signal drifts to temperature changes and detection of possibly non-investigated sources of fluctuations in the electric field or dielectric constant of the surrounding.

Another possible source for signal drifting might be the lack of regulation of the supply voltage. Possibly, monitoring of the supply voltage and / or the use of better regulated power supplies can do the trick. Additionally, if the regulation circuit of the power supply unit depends somewhat on the temperature, then the signal could be temperature dependent, even if the oscillator circuits were not, which could be difficult to handle if rudimentary fan speed control is inherent to the power supply that affects the temperature of the supply unit in an undesired way.

5.2 Suggestions for the Improvement of the Data Processing Procedure

The code written for the translation of audio wave data to frequency versus time data depended on a criterium that took into consideration only two samples per wave cycle and outliers were simply assigned the mean value of the two adjacent samples.

This is not a scientifically exact method and could be improved by an algorithm that takes more samples of one wave cycle into account to evaluate its shape, starting and end points and ignoring sudden changes.

Alternatively, Fourier Transformation could be applied to every few fractions of a second of the audio data, then the frequency position of the lowest peak of the spectrum could be evaluated as the actual frequency at that time. This would come at the cost of a substantial reduction of the temporal resolution and increased calculation efforts (also meaning longer calculation times), but would probably be more correct and has the advantage that Fourier Transformation packages are available from open sources.

5.3 Suggestions for the Improvement of the Calibration of the Particle Circulation Rate

Potential improvements to the measurement method regarding the particle circulation mass flow include gravimetrical determination of the particle outflow from the outlet of the screw conveyor (e.g. weight-logging a vacuum cleaner connected instead of the riser) and the application of means to reduce the electrostatic effects. The latter include proper humidification of the air used for fluidization and adding conductive coating to either the particles or the particle loop walls, as suggested by D. Geldart [18].

While coating the particles would be a non-trivial task to do and, besides added efforts and possible risks related to health and environmental contamination, would probably change the particles' properties. If the coating is stripped by the vigorous inter particle and wall contacting, this would mean the properties would change over time in a way that is non-trivial to predict or keep track of.

Conductive coatings of the walls of the particle loop will most probably make them lose transparency, which was one of the main reasons the materials were chosen for. Analogously to the particles, wall coatings could be subject to wear and thus be only a temporary solution with gradually changing properties.

The mentioned gravimetric approach however could in fact be a viable alternative, provided proper means of time and weight data logging, however, theoretically videotaping a weight scale at a known frame rate would do.

References

[1] Jahnig C. E., Campbell D. L., and Martin H. Z. *Fluidization.* Plenum Press, 1st edition, 1980.

[2] Patil A. V. *Heat transfer in gas-solid fluidized beds.* Dissertation, Technische Universiteit Eindhoven, June 2015.

[3] Latif A. *A Study of the Design of Fluidized Bed Reactors for Biomass Gasification.* PhD thesis, University of London, Torrington Place, November 1999.

[4] Hofbauer H. Übersicht über industrielle Anwendungen der Wirbelschichttechnik. Lecture notes, TU Wien, Vienna, Summer Term 2012.

[5] Zhuang Y., Chen X., and Liu D. Stochastic bubble developing model combined with markov process of particles for bubbling fluidized beds. *Chemical Engineering Journal*, 291:206 – 214, 2016.

[6] Wei X., Sheng H., and Tian W. Characterizing particle dispersion by image analysis in icfb. *International Journal of Heat and Mass Transfer*, 49(19):3338 – 3342, 2006.

[7] Gidaspow D. *Multiphase Flow And Fluidization.* Academic Press, Harcourt Press and Company, 1994.

[8] Wang T., He Y., and Kim D. R. Granular temperature and rotational characteristic analysis of a gas–solid bubbling fluidized bed under different gravities using discrete hard sphere model. *Powder Technology*, 271(Supplement C):35 – 48, 2015.

[9] Guío Peréz D. C. *Cold flow model assisted evaluation of an improved dual circulating fluidized bed design for chemical looping*

processes including solids residence time measurements. PhD thesis, TU Wien, Vienna, September 2013.

[10] Fan L.-S. *Gas-Liquid-Solid Fluidization Engineering*, page 763. Butterworths Series in Chemical Engineering. Butterworth Publishers, division of Reed Publishing, 1989.

[11] Molerus O. Fluid mechanics and heat transfer in fluidized beds. *KONA Powder and Particle Journal*, 18:121–130, 2000.

[12] Sette E. *Solids mixing in bubbling fluidized beds.* PhD thesis, Chalmers University of Technology, Göteborg, Sweden, 1999.

[13] Kuipers J. A. M., Prins W., and Van Swaaij W. P. M. Numerical calculation of wall-to-bed heat-transfer coefficients in gas-fluidized beds. *AIChE Journal*, 38(7):1079–1091, 1992.

[14] Kunii D. and Yagi S. Fluidized-solids reactors with continuous solids feed -i, residence time of particles in fluidized beds. *Chemical Engineering Science*, 16:364–371, January 1961.

[15] Werther J. Measurement techniques in fluidized beds. *Powder Technology*, 102:15–36, 1999.

[16] Sanderson J. and Lim K. Unpublished paper: Inductance techniques for use in fluidized beds. May 2016.

[17] Earle J. L. Pulse induction metal detector having high energy efficiency and sensitivity, January 19 2010. US Patent 7,649,356.

[18] Geldart D. Types of gas fluidization. *Powder Technology*, 7:285–292, November 1972.

[19] Hofbauer H. Wirbelschichttechnik. Lecture notes, TU Wien, Vienna, Summer Term 2013.

[20] Gibilaro L. G. *Fluidization Dynamics.* Butterworth-Heinemann, 225 Wildwood Avenue, Woburn MA 01801-2041, 2001.

[21] Grace J. R. and Bi H. *Circulating Fluidized Beds.* Blackie Academic and Professional, 1st edition, 1997.

[22] Wen C. Y. and Yu Y. H. A generalized method for predicting the minimum fluidization velocity. *AIChE Journal*, 12(3):610–612, 1966.

[23] Grace J. R. Fluidized-bed hydrodynamics. In Hetsroni G., editor, *Handbook of Multiphase Systems*. 1982.

[24] Kunii D. and Levenspiel O. *Fluidization Engineering*. Butterworth-Heinemann, 80 Montvale Avenue, Stoneham, MA 02180, 2nd edition, 1991.

[25] Pell M. Gas fluidization. *The Canadian Journal of Chemical Engineering*, 69(1):398–399, 1991.

[26] Fogler H.S. *Elements of Chemical Reaction Engineering*. Prentice-Hall of India, 3rd edition, 1999.

[27] Levenspiel O. *Chemical Reaction Engineering*. John Wiley & Sons, Oregon State University, Corvallis, OR, 97331, 3rd edition, 1999.

[28] Poyser W.A. *Magnetism and Electricity: A Manual for Students in Advanced Classes*. Longmans, Green & Co., 1892.

[29] Mania A.J. Assis A.K.T., Rodrigues Jr.W.A. The electric field outside a stationary resistive wire carrying a constant current. *Foundations of Physics*, 29(5):729–753, February 1999.

[30] Goldblatt W.M. *Electromagnetic Induction Sensing of Individual Tracer Particles in a Circulating Fluidized Bed*. PhD thesis, University of British Columbia, October 1990.

[31] Moreland C. W. BFO theory, 1999.

[32] Quirollari R., Hoxha R., and Nguyen W. T. Wideband voltage controlled oscillator (VCO) for RF applications. Bachelor Thesis, April 2016.

[33] Gottlieb I. M. *Practical Oscillator Handbook*. Elsevier Ltd., 1997.

[34] Smith D. How to make a metal detector. `http://www.easytreasure.co.uk/bfo2.htm`. Accessed: March 14th, 2018.

[35] Hofer G., Märzinger T., Eder C., Pröll F., and Pröll T. Particle mixing in bubbling fluidized bed reactors with continuous particle exchange. September 2018.

[36] Hofer G., Schöny G., and Pröll T. Acting on hydrodynamics to improve the local bed-to-wall heat transfer in bubbling fluidized beds. *Chemical Engineering Research and Design*, 135:309–318, April 2018.

Acronyms

AC alternating current.

BFO beat frequency oscillator.

CFB circulating fluidized bed.

CSTR continuously stirred tank reactor.

DC direct current.

HF high frequency.

PC personal computer.

PFR plug flow reactor.

PLU programmable logic controller.

PVC polyvinyl chloride.

RTD residence time distribution.

Notation

A area.

A_p surface area of a particle mass.

Ar Archimedes number.

$A_{s,Veq}$ surface area of a sphere with a volume that corresponds to that of an average particle.

C electric capacitance.

$C(t)$ time dependent concentration curve.

C_D fluid dynamical drag coefficient.

Δ finite differences prefix.

d_i mesh size of a sieve interval in sieving analysis.

d_p mean equivalent particle diameter.

$\bar{d}_p$ mean Sauter diameter.

d_S mean equivalent particle diameter related to surface area.

d_{SV} mean equivalent particle diameter related to surface area.

d_V mean equivalent particle diameter related to volume.

ϵ bed voidage.

$E(t)$ differential residence time function.

f frequency.

fs sample rate of an audio file.

$F(t)$ integral residence time function.

g gravitational acceleration.

γ gamma radiation.

Δh height difference.

$\mathbf{L}$ electromagnetic inductivity.

L_1 wave length of a first wave signal.

L_2 wave length of a second wave signal.

L_{beat} wave length of a beat wave.

m_{bed} bed mass.

$\dot{m}$ mass flow.

μ dynamic viscosity.

N_0 total amount of tracer material.

Δp pressure difference.

ϕ shape correction factor.

π circle geometry constant.

Q transistor.

R resistive component of an electric circuit.

Re Reynolds number.

ρ_b bulk density.

ρ_f fluid density.

ρ_p inner particle density.

t time.

τ mean residence time.

τ_{CSTR} characteristic time parameter of continuously stirred tank reactors.

τ_{PFR} characteristic delay time of idealized plug flow reactors.

$\bar{t}$ First momentum of a residence time distribution.

u_f superficial velocity.

u_{mb} minimum bubbling velocity.

u_{mf} minimum fluidization velocity.

u_t minimum velocity where solid entrainment occurs.

V volume.

$\dot{V}$ volumetric flow.

V_{bed} bed bulk volume.

V_p volume occupied by a particle mass.

V_{void} inter particle volume.

x_i mass fraction of a sieve interval in sieving analysis.

y array of sample values of an audio file.

List of Figures

1 Geldart particle regimes and their discrimination conditions in 2 dimensional field of density difference between particles and fluid versus particle size. 7

2 Progression of the pressure difference between the vertical bed limits through the stages of fluidization. 8

3 Drag coefficient in a range of particles' Reynolds numbers. 11

4 Differential RTD with $\bar{t}$ being the first momentum of the distribution, calculated according to (16). 13

5 Cumulative RTD with the median residence time being read from the horizontal position of the intersection of the cumulative function with the vertical position of 0.5 of the total amount of tracer material (having lower and equally higher residence times). . . 13

6 RTD outcomes of idealized and axially dispersive PFRs (a) as well as that of idealized CSTRs and of a series of an idealized PFR and an idealized CSTR (b) with indication of the characteristic parameters as provided by H. S. Fogler [26]. 16

7 Problems of real mixed-type reactors and their causes, taken from O. Levenspiel [27]. 17

8 Magnetic field lines run circularly around each wire in direction of a right handed thread and interfere to form a linear field in the center of the coil. 18

9 Tank circuit as an electrical resonator. 21

10 When two continuous sine waves with relatively short primary wave lengths L_1 and L_2 that differ only by a small fraction of their length are added, then a secondary beat wave with a relatively long wavelength L_{beat} results. 23

11 BFO circuit with some parts being specific to the reference oscillator (L1, C1-2, Q1), some to the measurement oscillator (L2, C3-4, Q2), R2 and R4 making up the signal mixer, the central region (Q3-6, R5-10, C5-9) accounting for amplification and shaping of the output signal plus portioning and phase adjustment of the feedback signal and the rightmost region being a measurement transformer that converts the output frequency to a DC voltage. 27
12 A small snippet of wave data read from the recorded file with points marked where one sample is below and the next sample is at or above a certain threshhold. . 29
13 The 3D-printed coil holder containing the coil in the groove between the two external rings. 32
14 Reference coil assembly including the coil holder (1), a threaded pole (2) that moves the ferrite core (3) into or out of the coil interior (4). 33
15 Drawing of the small scale fluidization pipe with its functional features being the windbox (1), gas distributor (2), consisting of a hole drilled acrylic glass plate and a fabric filter attached to its lower surface, fluidization chamber (3) and also depicting the possible measurement arrangements, such as a coil being mounted around the inner PVC pipe (5) either in lower position (4) or higher position (7), in the latter case it was supported by an adjustable acrylic glass ring (6). An outer acrylic glass pipe (8) is mounted on top, containing the upper section of the bed and the freeboard (9), which is limited on top by a fabric off gas filter (10). 34
16 3D-view of the cold flow model assembly from its rear side, depicting the fluidized bed chamber (1), the freeboard (2), the freeboard's off-gas filter (3), the particle removal pipe (4), the screw conveyor (5), the riser pipe (6), the particle separator (7) and the particle return pipe (8). The direction of movement of the particles in the loop is indicated by red arrows. . . . 36

17 Sketch of the front view of the fluidized bed chamber, showing the dead end gas inlet pipe (1) with its ventilation slits (2) that feed the windbox, whose only exit is the gas distributor plate (3) which provides the primary gas flow for the fluidization chamber (4). All the mounting positions for crossing pipes were sealed with plugs (○). At the particle removal pipe (5), solids exit the fluidization chamber and descend to enter the screw conveyor (6). After passing the particle loop, the solids return to the chamber via the downcomer pipe (7). At both, solids removal and return pipes, measurement coils (8) were mounted. . 37
18 Sketched piping scheme of the pressurized air supply of the cold flow model device, beginning with the compressor in the far left of the Figure, proceeding to the bypass pipe and pressure reducers via filters and the buffer tank. Every branch including the bypass has a manual regulation valve for air flow control with the only exception being the fluidization chamber, where the manual valve is only for opening the branch and the regulation is done by a motorized ball valve. 39
19 Calibration data of the mass flow of particles in dependency of the volumetric air flow through the pneumatic motor of the screw conveyor. The error bars represent standard deviation. 42
20 Calibration graph of the BFO device, showing the frequency deflection in dependency of the ferrite content. 43
21 Increase of bed voidage caused by bubbling fluidization at various superficial velocities in both coil positions, low and high. The error bars represent standard deviation. 45
22 Raw data of exemplary measurement runs for both coil position at the same fluidization velocity, illustrating the differences in bubble size and thereby fluctuation of tracer concentration in the coil. 46
23 Raw data of the peak measured at the inlet upon the injection of ferritic tracer material. 47

24 Time dependent concentration of tracer material captured in the course of an RTD measurement run with $u/u_{mf} = 9.26$ and a solids circulation rate of 186 kg/h. 48
25 Drift subtracted and transformed E(t) data featuring the median residence time and combined idealized PFR and CSTR model as well as its characteristic parameters. $u/u_{mf} = 9.26$, solids circulation rate: 186 kg/h. 49
26 Progression and convergence of the parameters τ_{CSTR} and τ_{PFR} in the progress of the iterative model fitting. 50
27 Cumulative RTD. 51
28 Layout of the printed circuit board. 67
29 Output sheet of the volume related particle size distribution of the used glass beads as produced by the Mastersizer2000 device by Malvern Instruments. . . . 68

Listings

1 Arrangement of functionally relevant code that was used to quantify the frequency of each wave cycle from waveform data 30
2 R output of the summary of the linear calibration model regarding the particle mass flow through the particle loop. 41
3 R output summarizing the fit of the linear calibration model to the measured frequency deflection in dependency of the ferrite content of the particle mix within the coil. 44
4 R output summarizing the fit of the delayed exponential model to the tracer concentration measurement curve. 51

List of Tables

1 Raw frequency data of the BFO calibration runs. . . 65
2 Raw frequency data of the bed expansion experiment. 65

3 Raw data of the particle circulation calibration experiment, showing the particle height level in the blocked downcomer pipe and the time elapsed since the first marking had been reached. 66

6 Appendix

Table 1: Raw frequency data of the BFO calibration runs.

ferrite content $[g/g]$	$f_{before}[Hz]$	$f_{while}[Hz]$	$f_{after}[Hz]$
empty vessel	303.05	309.57	304
bare glass beads	306.92	315.32	309.84
0.00046	339.81	332.19	341.54
0.00296	352.05	339.69	351.82
0.00183	348.45	338.63	348.76
0.00800	365.01	344.51	367.38
0.01270	377.74	345.28	377.89
0.02292	401.33	347.93	402.46
0.03218	417.07	350.68	417.31
0.05360	459.14	352.3	460.21
0.06521	480.92	353.62	481.12
0.07691	511.12	356.36	510.95
0.09297	547.89	358.03	547.21
0.1082	577.37	361.52	578.7

Table 2: Raw frequency data of the bed expansion experiment.

$u[m/s]$	coil position	$f_{before}[Hz]$	$f_{while}[Hz]$	$sd_{while}[Hz]$	$f_{after}[Hz]$
0.0283	low	906.7	907.7	0.5	908.9
0.0315	low	912.3	909	0.6	912.8
0.0524	low	897.9	891.8	1.2	899.3
0.0577	low	899.1	892.4	1.3	900.3
0.0734	low	893.2	885.9	1.8	895.8
0.0839	low	895.2	888	2	898.7
0.0944	low	899.5	889.9	2.8	900.5
0.1049	low	900.3	891.5	3.3	901.1
0.0283	high	883	882	0.5	882.6
0.0419	high	881.1	879.3	1.5	882.6
0.0524	high	882.9	881.5	2.3	886.1
0.0629	high	885.6	881.7	4.6	887.9
0.0734	high	888	880.6	6.9	889.9
0.0839	high	890	879.8	10.8	892.8
0.0944	high	893.2	876.9	12.5	889.9

Table 3: Raw data of the particle circulation calibration experiment, showing the particle height level in the blocked downcomer pipe and the time elapsed since the first marking had been reached.

	8 [Nm/h]		10 [Nm/h]		12 [Nm/h]		14 [Nm/h]	
repetition	time [s]	height [m]	time [s]	height [m]	time [s]	height [m]	time [s]	height [m]
1	8.67	0.05	3.93	0.05	5.33	0.05	3.20	0.05
	18.13	0.10	10.87	0.10	11.33	0.10	6.47	0.10
	47.00	0.30	19.13	0.15	17.80	0.15	9.20	0.15
	54.00	0.35	36.67	0.30	29.47	0.30	20.80	0.30
	64.33	0.40	39.60	0.35	34.53	0.35	25.73	0.35
	72.67	0.45	41.07	0.40	40.87	0.40	30.40	0.40
	82.33	0.50	43.67	0.45	46.60	0.45	33.87	0.45
			49.07	0.50	52.53	0.50	37.87	0.50
2	4.67	0.05	3.67	0.05	2.60	0.05	3.87	0.05
	12.00	0.10	10.33	0.10	17.80	0.20	8.67	0.10
	34.67	0.30	17.73	0.15	22.00	0.25	20.00	0.25
	41.33	0.35	36.87	0.30	26.07	0.30	25.80	0.30
	50.67	0.40	41.13	0.35	30.93	0.35	29.87	0.35
	57.93	0.45	42.67	0.40	36.27	0.40	34.00	0.40
	65.67	0.50	43.27	0.45			38.60	0.45
			48.67	0.50				
3	4.33	0.05	6.13	0.05	5.80	0.05	5.00	0.05
	41.93	0.30	14.00	0.10	11.47	0.10	17.93	0.20
	48.00	0.35	21.67	0.15	17.13	0.15	22.40	0.25
	52.33	0.40	38.40	0.30	31.60	0.30	24.53	0.30
	58.53	0.45	42.93	0.35	33.33	0.35	28.60	0.35
	65.67	0.50	50.13	0.40	35.33	0.40	31.47	0.40
			57.33	0.45	38.33	0.45		
			64.33	0.50	43.33	0.50		
4	7.67	0.05	6.87	0.05	4.40	0.05	3.80	0.05
	14.00	0.10	20.27	0.15	9.73	0.10	18.67	0.20
	23.00	0.15	34.20	0.30	26.33	0.25	23.00	0.25
	41.47	0.30	41.53	0.35	31.27	0.30	28.40	0.30
	47.20	0.35	47.00	0.40	35.73	0.35	33.07	0.35
	52.00	0.40	52.87	0.45	40.33	0.40	35.33	0.40
	54.20	0.45	57.07	0.50	46.07	0.45		
	58.20	0.50						
5	9.00	0.05	5.40	0.05	4.53	0.05	3.73	0.05
	18.00	0.10	15.73	0.20	8.67	0.10	8.07	0.10
	40.00	0.25	20.73	0.25	25.40	0.25	20.00	0.25
	48.00	0.30	28.00	0.30	30.40	0.30	23.73	0.30
	56.20	0.35	35.13	0.35	35.60	0.35	26.20	0.35
	63.00	0.40	41.00	0.40	39.40	0.40	28.20	0.40
	69.20	0.45			40.67	0.45	32.00	0.45
6	6.93	0.05	7.07	0.05	5.07	0.05	4.93	0.05
	15.67	0.10	12.40	0.10	18.67	0.20	9.20	0.10
	42.33	0.30	29.87	0.25	23.93	0.25	22.40	0.25
	48.07	0.35	36.80	0.30	29.87	0.30	25.13	0.30
	51.67	0.40	41.80	0.35	34.93	0.35	30.20	0.35
	53.33	0.45	46.13	0.40	40.60	0.40	35.53	0.40
	57.93	0.50	48.80	0.45			39.40	0.45
7					4.93	0.05	4.80	0.05
					10.00	0.10	18.33	0.20
					23.40	0.25	21.73	0.25
					28.60	0.30	26.07	0.30
					34.20	0.35	29.33	0.35
					39.87	0.40	33.60	0.40
					43.67	0.45		

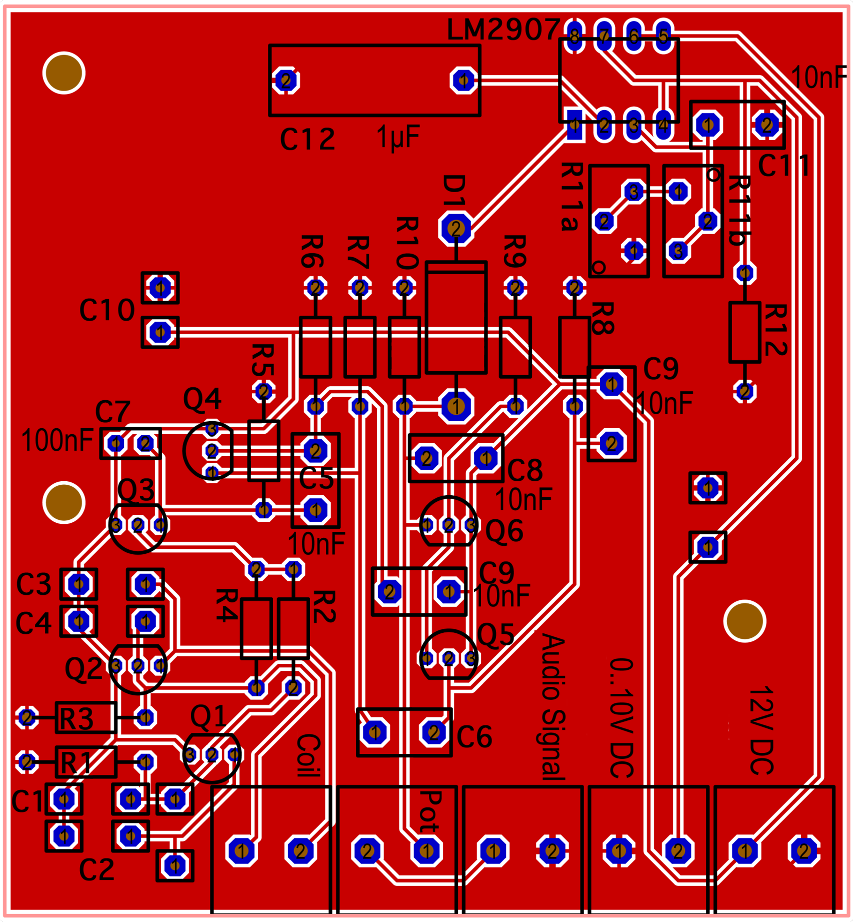

Figure 28: Layout of the printed circuit board.

MASTERSIZER 2000

Analyse Report

Probenname: Glasperlen used **SOP Name:** Glasperlen Microrinne **Gemessen:** Tuesday, February 23,
Probenherkunft: Factory **Operator:** tlaminger **Berechnet:** Tuesday, February 23,
Probenreferenz: **Datenursprung:** Gemittelt

Probenmaterial: Glass beads (typical) **Dispergiermodul:** Scirocco 2000 (B) **Abschattung:** 0.58 %
Partikel RI: 1.520 **Absorption:** 0 **Analysemodell:** Monomodale Verteilung (fein)
Dispergierfluid: **Meßbereich:** 0.020 to 2000.000 um **Fit(gewichtet):** 0.704 %
Fluid RI: 1.000 **Emulation:** Aus

Konzentration: 0.0025 %Vol **Vol. Mittelwert D[4,3]:** 145.035 um **Spezifische Oberfläche:** 0.0188 m^2/g
Breite : 0.716 **Gleichförmigkeit:** 0.226 **D[3,2]:** 130.488 um
Verteilungsart: Volumen

d(0.1): 97.556 um **d(0.5):** **141.952** um d(0.9): 199.220 um

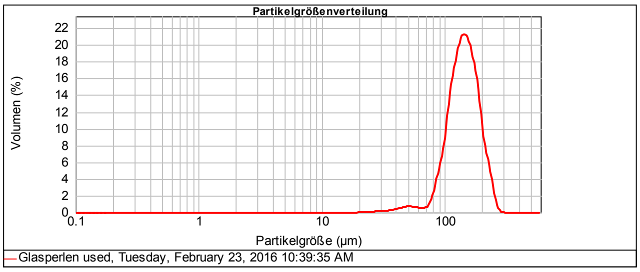

Größen-	Häufigkeit (%)	Größen-	Häufigkeit (%)	Größen-	Häufigkeit (%)	Größen-	Häufigkeit (%)	Größen-	Häufigkeit (%)	Größen-	Häufigkeit (%)
0.020	0.00	0.142	0.00	1.002	0.00	7.096	0.00	50.238	0.54	355.656	0.00
0.022	0.00	0.159	0.00	1.125	0.00	7.962	0.00	56.368	0.46	399.052	0.00
0.025	0.00	0.178	0.00	1.262	0.00	8.934	0.00	63.246	0.40	447.744	0.00
0.028	0.00	0.200	0.00	1.416	0.00	10.024	0.00	70.963	0.79	502.377	0.00
0.032	0.00	0.224	0.00	1.589	0.00	11.247	0.00	79.621	2.80	563.677	0.00
0.036	0.00	0.252	0.00	1.783	0.00	12.619	0.00	89.337	4.94	632.456	0.00
0.040	0.00	0.283	0.00	2.000	0.00	14.159	0.00	100.237	9.44	709.627	0.00
0.045	0.00	0.317	0.00	2.244	0.00	15.887	0.00	112.468	13.16	796.214	0.00
0.050	0.00	0.356	0.00	2.518	0.00	17.825	0.00	126.191	15.57	893.367	0.00
0.056	0.00	0.399	0.00	2.825	0.00	20.000	0.02	141.589	15.91	1002.374	0.00
0.063	0.00	0.448	0.00	3.170	0.00	22.440	0.07	158.866	14.09	1124.683	0.00
0.071	0.00	0.502	0.00	3.557	0.00	25.179	0.08	178.250	10.65	1261.915	0.00
0.080	0.00	0.564	0.00	3.991	0.00	28.251	0.11	200.000	5.86	1415.892	0.00
0.089	0.00	0.632	0.00	4.477	0.00	31.698	0.16	224.404	3.29	1588.656	0.00
0.100	0.00	0.710	0.00	5.024	0.00	35.566	0.24	251.785	0.57	1782.502	0.00
0.112	0.00	0.796	0.00	5.637	0.00	39.905	0.37	282.508	0.00	2000.000	
0.126	0.00	0.893	0.00	6.325	0.00	44.774	0.51	316.979	0.00		
0.142		1.002		7.096		50.238		355.656			

Kommentar: *Mittelwert*

Malvern Instruments Ltd.
Malvern, UK
Tel.: +44 (0) 1684-892456; Fax: +44 (0) 1684-892789

Mastersizer 2000 Version 5.12G
S/N: MAL1034369

Dateiname: knorr bremse.mea
Messdatensatz-Nr.: 639
23 Feb 2016 10:45:27 AM

Figure 29: Output sheet of the volume related particle size distribution of the used glass beads as produced by the Mastersizer2000 device by Malvern Instruments.